Chapter 3

Titration

In this chapter, I will describe several methods and applications of calculating the titration behavior of proteins, *i. e.* the protonation probability of each of their titratable groups at different pH values. Together with titratable groups, also redox groups are treated here, since redox titration is in principle very similar to conventional pH titration. The chapter starts with the titration of single, rigid protein structures and proceeds with different methods of introducing conformational flexibility in the calculations.

All methods are illustrated by applications to bacterial photosynthetic reaction centers and myoglobin. The results presented here include also energetics of electron and proton transfer reactions and show implications of protonation and conformational changes for protein function.

3.1 Titration of a single, rigid protein structure

3.1.1 To be investigated: bacterial photosynthetic reaction centers

The investigation of photosynthetic proteins is one of the major research interests of the Knapp group members (Muegge *et al.*, 1995; Ullmann & Kostić, 1995; Muegge *et al.*, 1996; Apostolakis *et al.*, 1996; Ullmann *et al.*, 1997, 1997; Rabenstein *et al.*, 1998b, 1998a; Ullmann *et al.*, 2000). Thus it is not surprising that we chose as the area of application the bacterial photosynthetic reaction centers (bRCs) of the purple bacteria *Rhodopseudomonas (Rps.) viridis* and *Rhodobacter (Rb.) sphaeroides*. The bRCs are pigment-protein complexes in the membrane of the purple bacteria. They convert light energy into electrochemical energy by coupling photo-induced electron transfer to proton uptake from cytoplasm. The x-ray structure of the bRCs from *Rps. viridis* (Deisenhofer *et al.*, 1985, 1995; Lancaster & Michel, 1997, 1999) and from *Rb. sphaeroides* (Allen *et al.*, 1987; Chang *et al.*, 1991; Ermler *et al.*, 1994; Arnoux *et al.*, 1995; Stowell *et al.*, 1997) enabled a more detailed understanding of the various functional processes in the bRC. The present work deals with the most recent x-ray structures from Lancaster and Michel (1999)[1] and Stowell *et al.* (1997). Three polypeptides, the L, H, and M subunits, form the protein complex. Common to both bRCs are the following cofactors: four bacteriochlorophylls, two bacteriopheophytins, one non-heme iron and two quinones. The primary quinone Q_A is a menaquinone (MQ) in the bRC from *Rps. viridis*, but a ubiquinone (UQ) in the bRC from *Rb. sphaeroides*. The secondary quinone Q_B is a UQ in both types of bRC. The structure of the bRC from *Rps. viridis* contains as an additional cofactor a carotenoid, which is missing in the R-26 strain used for the structure of the bRC from *Rb. sphaeroides*. A four-center *c*-type cytochrome with

[1] Actually, partially the results in this work are based on another structure of the bRC from *Rps. viridis*. We derived this structure from the coordinates of Deisenhofer *et al.* (1995), but it resembles closely the more recent structure of Lancaster and Michel (1999) (for details see Rabenstein *et al.* (1998b) and Rabenstein and Knapp (2000b)). Several test calculations showed that both structures yield extremely similar results.

four hemes as cofactors is tightly bound to the bRC from *Rps. viridis* (Figure 3.1), but missing in *Rb. sphaeroides.* The cofactors are arranged in the two branches A and B related by a C_2 symmetry

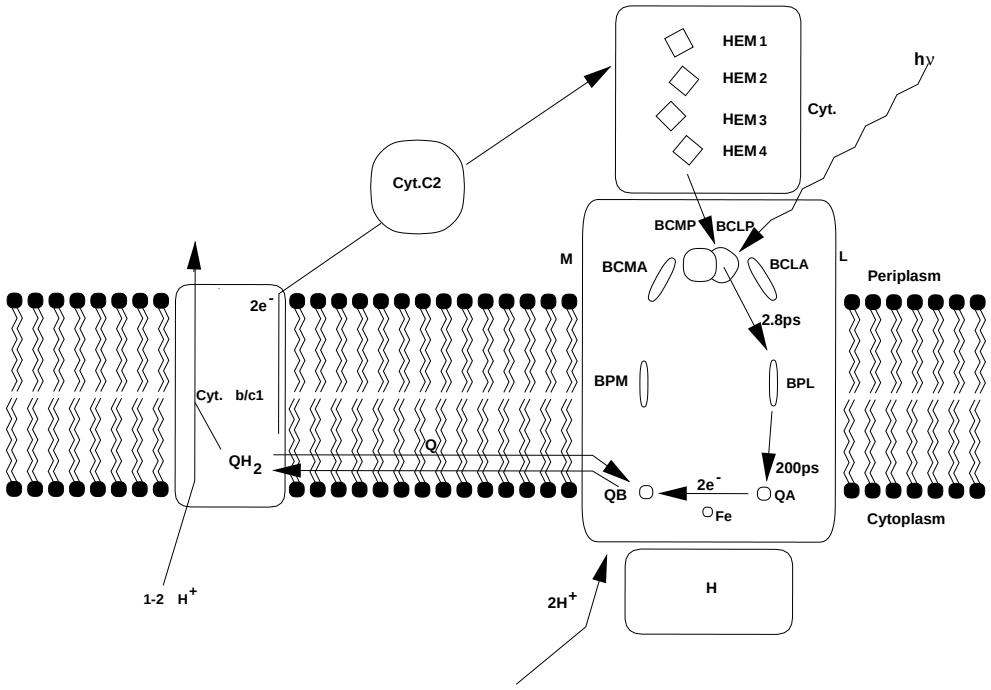

Figure 3.1: Cartoon of the bRC from *Rps. viridis* together with the membrane complex cytochrome bc_1 and the soluble cytochrome c_2 (Stroop, 1993)

and extend from the special pair to the quinones. Only the A-branch is electron-transfer active. Its cofactors are predominantly embedded in the L subunit. Electronic excitation of the special pair, a bacteriochlorophyll dimer, induces a multi-step electron transfer process from the special pair to the primary quinone Q_A. From there the electron moves to the secondary quinone Q_B. After this initial reaction, a second electron transfer from Q_A to Q_B and two protonations of Q_B follow, resulting in a dihydroquinone Q_BH_2. The dihydroquinone leaves its binding site and is replaced by an oxidized UQ from the quinone pool (see Figure 3.6 on page 49). The temporal order of these reactions was, however, a long time not completely resolved (for a review see Okamura and Feher (1992)). Recently, Graige *et al.* (1996) proposed several models for the coupling of the protonation of Q_B to the electron transfer between Q_A and Q_B. Based on their kinetic data, they favored either a mechanism in which the second electron transfer to Q_B occurs in a concerted manner with the first protonation of Q_B or a mechanism in which the first protonation of Q_B precedes the second electron transfer. This hypothesis, which seems to be well established in the meantime, was supported also by our own work (Rabenstein *et al.*, 1998b) as reported later in this chapter. As an additional complication, the dihydroquinone Q_BH_2 has two acidic protons, one at the quinone oxygen atom proximate to the non-heme iron (near His-L190), the other at the quinone oxygen atom distant from the non-heme iron (near Ser-L223). Thus, there are two possibilities for the first protonation of Q_B, which were also discussed in our work (Rabenstein *et al.*, 1998b).

In the center of our interest are the protonation and redox reactions of the two quinones. By using the methods described in the next section, we want to investigate the coupling between the electron-transfer reactions (of the quinones) and the protonation reactions (of the quinones as well as of the remaining titratable groups) in the bRC. We do this mainly for the bRC from *Rps. viridis.* On the basis of the light-exposed and the dark-adapted x-ray structures of the bRC from *Rb. sphaeroides* (Stowell *et al.*, 1997), we study another interesting feature of the first electron transfer from $Q_A^{\cdot -}$ to Q_B. The

rate of this electron transfer at low temperatures is dramatically increased in bRC frozen under illumination compared to bRC frozen in the dark (Kleinfeld *et al.*, 1984b). This effect suggests that the dark-adapted and the light-exposed bRCs differ in their conformation, and the dark-adapted state has to undergo a conformational change before electron transfer can take place efficiently. This conformational change may occur much slower than the electron transfer, which would lead to conformational gating of the reaction (Davidson, 1996). Conformational gating occurs also in other electron transfer proteins (Zhou & Kostić, 1993) and was proposed for the bRC on the basis of a driving force assay (Graige *et al.*, 1998). Indeed, the x-ray structure (Stowell *et al.*, 1997) of the dark-adapted bRC from *Rb. sphaeroides* shows that Q_B is displaced by approximately 5 Å and has undergone a 180° propeller twist compared to the structure of the light-exposed bRC (Figure 3.2). The binding site of Q_B in the dark-adapted bRC is referred to as the distal binding site (with respect to the non-heme iron), whereas the binding site of Q_B in the light-exposed bRC is referred to as the proximal binding site. The goal of our work is to investigate the conformational gating hypothesis and to understand how the protein accomplishes the conformational gating.

3.1.2 Methods

3.1.2.1 Preparation of structures

In our calculations, we used the dark-adapted and light-exposed x-ray structures of the bRC from *Rb. sphaeroides* (Stowell *et al.*, 1997) with a resolution of 2.2 Å (PDB entry 1aij) and 2.6 Å (PDB entry 1aig), respectively, and the x-ray structure of the bRC from *Rps. viridis* (Lancaster & Michel, 1999) with a resolution of 2.45 Å (PDB entry 2prc). We considered only the first reaction center in the unit cell of the structures from *Rb. sphaeroides* (H, L, and M chain together with their cofactors) and ignored the other (N, O, and P chain in 1aig, R, S, and T chain in 1aij). Since the cytochrome *c* subunit in the structure from *Rps. viridis* is more than 25 Å away from the quinone binding sites, we neglected this subunit in our calculations. All water molecules, sulfate ions, and detergent molecules were removed from all used x-ray structures. The influence of water was considered exclusively by a higher dielectric constant in the resulting cavities and outside the protein as described in chapter 1. In some recent applications, selected water molecules were explicitly included in pK_a-calculations (Cometta-Morini *et al.*, 1993; Sampogna & Honig, 1994; Gibas & Subramaniam, 1996). These calculations yielded results different from those obtained without explicit water molecules. Different selection schemes for the water molecules were applied. Only a few crystal water molecules, all crystal water molecules, or even additional solvent molecules placed by modeling procedures were included. For hen egg lysozyme, the agreement between calculated and measured pK_a-values was better without explicit water molecules (Gibas & Subramaniam, 1996). Calculations without explicit water may agree better with experiments because the orientation of water molecules is not known from x-ray crystallography but is needed for these calculations. Since the orientation of water molecules is uncertain, we decided to remove all water molecules. We used an extended atom representation for most non-polar hydrogen atoms, except for the quinones, the chlorophylls, and the pheophytins, for which all hydrogens were treated explicitly. Polar hydrogens were also treated explicitly, with the exception of the acidic hydrogens of protonated glutamates and aspartates, which were represented by symmetrical charge adjustment of the two carboxyl oxygen atoms (see below). Coordinates of explicitly treated hydrogen atoms were generated with CHARMM (Brooks *et al.*, 1983). The positions of hydrogen atoms were energetically optimized, while the heavy atom positions were fixed. For this optimization, all titratable groups were in their standard protonation (*i. e.*, aspartate, glutamate, and the C-termini unprotonated, arginine, cysteine, histidine, lysine, tyrosine and the N-termini protonated), and both quinones were in their oxidized (uncharged) state.

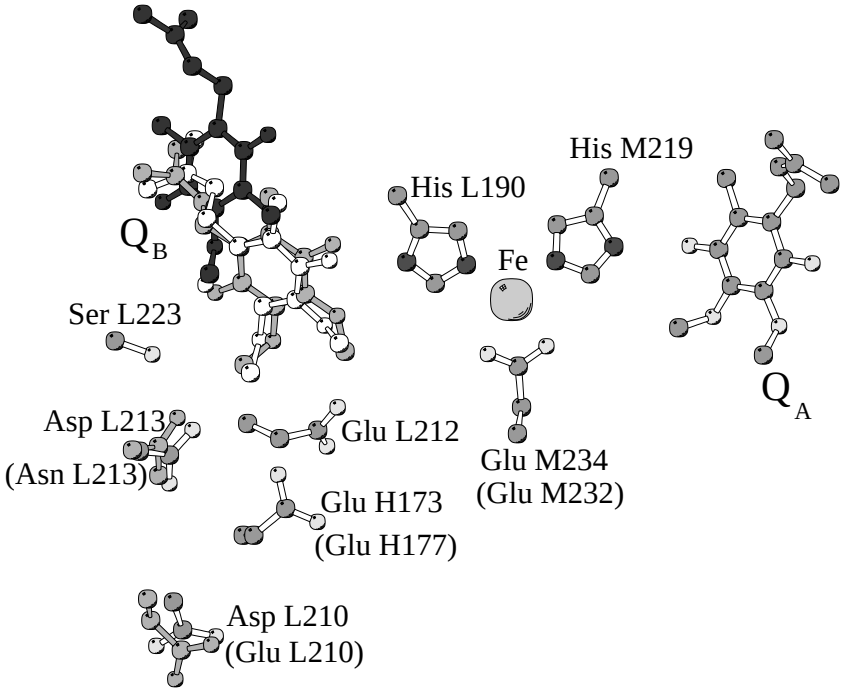

Figure 3.2: Q_B binding site of different bRC structures. The structures were superimposed with the Kabsch algorithm (Kabsch, 1976) considering all displayed molecular components except the two quinones and residue L210. The Q_B of the dark-adapted and light-exposed x-ray structures from *Rb. sphaeroides* (Stowell *et al.*, 1997) are displayed in black and white, respectively. Q_B from *Rps. viridis* (Lancaster & Michel, 1997, 1999) is depicted in gray. Residues common to all three structures are taken from the light-exposed x-ray structure of *Rb. sphaeroides*. Residues from *Rps. viridis* are denoted in brackets if named differently. If their position differs significantly, they are drawn in gray.

3.1.2.2 Atomic partial charges

Atomic partial charges of the amino acids, including the protonated and deprotonated states of titratable amino acids, were adopted from the CHARMM parameter set provided by MSI Inc. The acidic hydrogen atom of protonated glutamate and aspartate was not represented explicitly. Instead, appropriate charges were assigned symmetrically at the two carboxyl oxygen atoms. (This results in an atomic partial charge of -0.35 for each of the carboxyl oxygen atom in the protonated state.) The atomic partial charges, which are not included in the CHARMM parameter set, were calculated quantum-chemically with the program Spartan 4.0. (Wavefunction, Inc., Irvine, CA, 1995) We fitted the atomic partial charges to represent faithfully the electrostatic potential calculated from the wave functions using the CHELPG-like method (Breneman & Wiberg, 1990) implemented in Spartan (for details see Rabenstein (1997)). The atomic partial charges of chlorophyll and pheophytin (Figure 3.4) were calculated semiempirically at the PM3 level, those of the quinones (Figure 3.3) in all considered redox and protonation states, and of the deprotonated cysteine were calculated *ab initio* with the Hartree-Fock method using a 6-31G** basis set. The atomic partial charges of the high spin non-heme iron (Kartha *et al.*, 1991) and its ligands were calculated by a density functional method (LSDA/VWN) implemented in Spartan using the DN** basis. The calculated partial charges of the iron center and the two quinones are listed in Tables 3.1 to 3.4.

The carotenoid and the isoprene tails of the quinones, chlorophylls and pheophytins were not considered in the quantum chemical calculations. The atomic partial charges of these apolar groups were set to zero.

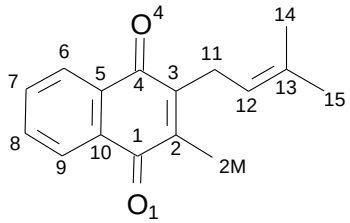

Menaquinone

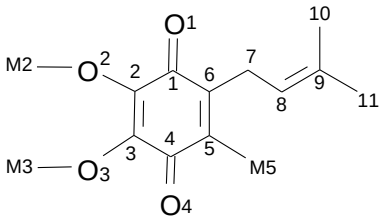

Ubiquinone

Figure 3.3: Atom names used for MQ and UQ in Tables 3.1 and 3.2.

3.1.2.3 The energy of a protonation state

The energy G^n of a protonation state n of a protein, which is characterized by the protonation state vector $\vec{x}_n = (x_1^n, x_2^n, \ldots, x_N^n)$, is given by eq 3.1 (Bashford & Karplus, 1990, 1991; Beroza *et al.*, 1991; Yang *et al.*, 1993; Beroza & Fredkin, 1996; Antosiewicz *et al.*, 1996; Ullmann & Knapp, 1999).

$$G^n = \sum_{\mu=1}^{N} \left((x_\mu^n - x_\mu^o) RT \ln 10 (\mathrm{pH} - \mathrm{p}K_{intr,\mu}) + \sum_{\nu>\mu}^{N} W_{\mu\nu} (x_\mu^n - x_\mu^o)(x_\nu^n - x_\nu^o) \right) \tag{3.1}$$

Table 3.1: Atomic partial charges for menaquinone (MQ), calculated *ab initio* by the Hartree-Fock method. Atom names are adopted from PDB-standard given in Figure 3.3. Hydrogen atoms are named according to their respective heavy atoms.

atom	$MQ^{\cdot -}$	MQ
C-1	0.35	0.54
O-1	-0.60	-0.50
C-2	-0.04	0.11
C-2M	-0.14	-0.33
3 H-2M	0.05	0.11
C-3	-0.32	-0.40
C-4	0.45	0.68
O-4	-0.63	-0.51
C-5	-0.08	-0.18
C-6	-0.10	-0.05
H-6	0.11	0.12
C-7	-0.17	-0.12
H-7	0.10	0.14
C-8	-0.19	-0.14
H-8	0.10	0.14
C-9	-0.08	-0.06
H-9	0.10	0.13
C-10	-0.07	-0.10
C-11	0.25	0.33
2 H-11	0.00	0.01
C-12	-0.43	-0.48
H-12	0.19	0.20
C-13	0.18	0.20
C-14	-0.33	-0.27
3 H-14	0.07	0.08
C-15	-0.03	-0.20
3 H-15	0.00	0.06

Table 3.2: Atomic partial charges for ubiquinone (UQ), calculated *ab initio* by the Hartree-Fock method. Atom names are adopted from PDB-standard given in Figure 3.3. Hydrogen atoms are named according to their respective heavy atoms.

atom	UQ^{2-}	$UQ^{\cdot -}$	UQ	$UQH^{-}_{prox.}$	$UQH^{-}_{dist.}$	$UQ{\cdot}H_{prox.}$	$UQ{\cdot}H_{dist.}$	UQH_2
C-1	0.45	0.52	0.65	0.55	0.23	0.54	0.27	0.26
O-1	-0.82	-0.62	-0.47	-0.73	-0.59	-0.42	-0.54	-0.54
H-1	—	—	—	—	0.37	—	0.41	0.41
C-2	-0.11	-0.12	-0.15	-0.15	-0.02	-0.04	0.04	-0.02
O-2	-0.36	-0.30	-0.27	-0.28	-0.32	-0.28	-0.34	-0.32
C-M2	0.26	0.12	-0.02	0.03	0.09	0.06	0.11	0.15
3 H-M2	-0.03	0.02	0.07	0.04	0.03	0.05	0.04	0.03
C-3	0.06	0.13	0.26	0.11	-0.01	0.16	0.08	0.09
O-3	-0.37	-0.33	-0.33	-0.32	-0.30	-0.34	-0.27	-0.30
C-M3	0.18	0.04	0.12	0.11	0.01	0.08	-0.06	0.05
3 H-M3	-0.01	0.04	0.04	0.02	0.04	0.05	0.08	0.05
C-4	0.26	0.28	0.38	0.06	0.35	0.10	0.38	0.10
O-4	-0.79	-0.57	-0.45	-0.57	-0.69	-0.52	-0.39	-0.54
H-4	—	—	—	0.37	—	0.41	—	0.41
C-5	-0.20	-0.03	0.15	0.11	-0.02	0.24	0.03	0.14
C-M5	0.21	-0.01	-0.30	-0.12	-0.14	-0.40	-0.27	-0.24
3 H-M5	-0.06	0.01	0.11	0.04	0.04	0.13	0.10	0.09
C-6	-0.41	-0.42	-0.42	-0.56	-0.44	-0.50	-0.31	-0.36
C-7	0.37	0.39	0.28	0.49	0.56	0.54	0.39	0.43
2 H-7	-0.04	-0.04	0.01	-0.06	-0.09	-0.06	-0.03	-0.04
C-8	-0.45	-0.50	-0.47	-0.55	-0.51	-0.52	-0.47	-0.52
H-8	0.20	0.21	0.18	0.24	0.22	0.20	0.19	0.21
C-9	0.16	0.26	0.28	0.25	0.22	0.20	0.21	0.29
C-10	-0.05	-0.16	-0.26	-0.21	-0.18	-0.07	-0.10	-0.30
3 H-10	0.02	0.07	0.10	0.05	0.05	0.10	0.09	0.08
C-11	-0.24	-0.38	-0.35	-0.24	-0.26	-0.33	-0.35	-0.30
3 H-11	-0.01	0.03	0.07	0.04	0.04	0.03	0.03	0.08

Table 3.3: Partial charges of the non-heme iron center calculated by a density functional (DFT) method. Charges of carbon bound hydrogens have been added to the charge of the respective carbon atom.

atom	charge
His-L190:	
C-β	-0.01
C-γ	0.28
C-δ2	-0.15
C-ε1	0.07
N-δ1	-0.32
H-δ	0.38
N-ε2	0.14
His-M217:	
C-β	0.00
C-γ	0.27
C-δ2	-0.15
C-ε1	0.15
N-δ	-0.38
H-δ1	0.38
N-ε2	0.11

atom	charge
His-M264:	
C-β	0.00
C-γ	0.22
C-δ2	-0.16
C-ε1	0.01
N-δ1	-0.28
H-δ	0.37
N-ε2	0.24
His-L230:	
C-β	-0.01
C-γ	0.23
C-δ2	-0.12
C-ε1	0.05
N-δ1	-0.33
H-δ	0.39
N-ε2	0.15

atom	charge
Glu-M232:	
C-β	-0.09
C-γ	0.18
C-δ	0.46
O-ε-1	-0.37
O-ε-2	-0.43
Fe	-0,28

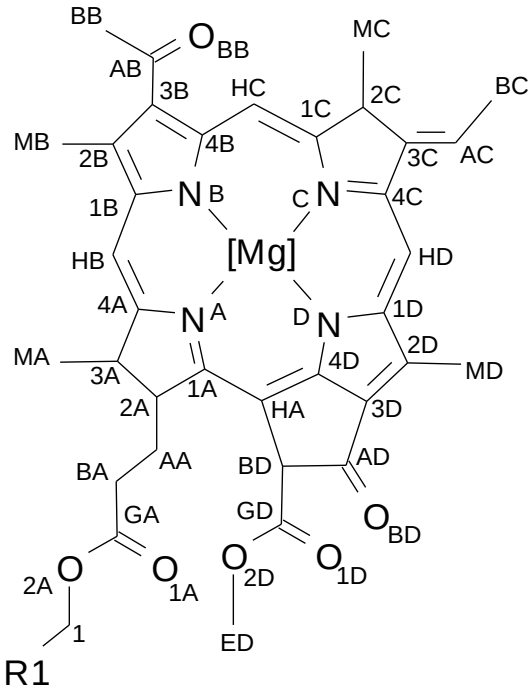

Figure 3.4: Atom names used for bacteriochlorophyll-b and bacteriopheophytin-b in Table 3.4.

Table 3.4: Atomic partial charges for bacteriochlorophyll-b and bacteriopheophytin-b, calculated by the semiempiric PM3 method. Atom names are adopted from PDB-standard given in Figure 3.4. Hydrogen atoms are named according to their respective heavy atoms.

atom	chlorophyll	pheophytin
Mg	0.10	—
N-A	0.11	-0.49
C-HA	-0.22	0.11
C-1A	0.03	-0.02
C-2A	0.10	0.14
H-2A	0.05	0.06
C-3A	-0.04	-0.22
H-3A	0.06	0.07
C-4A	-0.10	0.56
N-B	0.12	-0.50
H-B	—	0.36
C-HB	-0.20	-0.65
H-HB	0.19	0.21
C-1B	-0.05	0.44
C-2B	-0.16	-0.04
C-3B	-0.32	-0.39
C-4B	-0.02	0.40
N-C	0.01	-0.35
C-HC	-0.07	-0.46
H-HC	0.20	0.17
C-1C	-0.19	0.28
C-2C	0.24	0.17
H-2C	-0.01	0.02
C-3C	-0.12	-0.22
C-4C	0.05	0.17
N-DB	0.01	0.52
H-D	—	-0.01
C-HD	-0.13	-0.20
H-HD	0.18	0.20
C-1D	-0.06	-0.25
C-2D	0.18	0.05
C-3D	-0.41	-0.43
C-4D	0.21	-0.15

atom	chlorophyll	pheophytin
C-MA	0.01	0.00
3 H-MA	0.01	0.01
C-MB	0.11	-0.02
3 H-MB	-0.01	0.03
C-MC	-0.05	-0.09
3 H-MC	0.02	0.03
C-MD	-0.03	0.05
3 H-MD	0.03	0.01
C-AA	-0.13	0.06
2 H-AA	0.09	0.02
C-BA	-0.21	-0.30
2 H-BA	0.08	0.10
C-GA	0.77	0.79
O-1A	-0.53	-0.54
O-2A	-0.42	-0.43
C-1	0.15	0.19
2 H-1	0.01	0.01
C-AB	0.65	0.79
C-BB	-0.14	-0.41
3 H-BB	0.04	0.11
O-BB	-0.57	-0.52
C-AC	-0.18	-0.11
H-AC	0.08	0.07
C-BC	0.11	0.08
3 H-BC	0.00	0.00
C-AD	0.81	0.89
O-BD	-0.52	-0.55
C-BD	-0.73	-0.80
H-BD	0.29	0.30
C-GD	1.04	0.98
O-1D	-0.57	-0.53
O-2D	-0.50	-0.49
C-ED	0.19	0.27
3 H-ED	0.00	-0.02

Depending on the group μ, which can be protonated or unprotonated, x_μ^n adopts the values 1 or 0, respectively. $\vec{x}_o$ is the protonation state vector of the so-called reference state, where all titratable groups are in their uncharged protonation state, *i. e.* x_μ^o is 1 if μ is an acid and 0 if μ is a base. The sums run over all N titratable groups. $pK_{intr,\mu}$ is the so-called intrinsic pK_a value of the group μ, *i. e.* the pK_a value of group μ when all other titratable groups are in the reference state. $W_{\mu\nu}$ is the electrostatic interaction energy of the groups μ and ν if both are charged. pK_{intr} and the symmetrical W-matrix are both calculated by solving the PBE on a grid (Warwicker & Watson, 1982) as described in chapter 1. For doing this, we used the program MEAD (Bashford & Gerwert, 1992; Bashford, 1997).

Table 3.5: Groups considered as titratable with the pK_a values of their model compounds. The heme propionate is needed in section 3.3.

Titratable group	Model compound pK_a	Reference
Arginine	12.0	Nozaki and Tanford (1967)
Aspartate	4.0	Nozaki and Tanford (1967)
Cysteine	9.5	Nozaki and Tanford (1967)
Glutamate	4.4	Nozaki and Tanford (1967)
δ-Histidine	7.0	Tanokura (1983)
ε-Histidine	6.6	Tanokura (1983)
Lysine	10.4	Nozaki and Tanford (1967)
Tyrosine	9.6	Nozaki and Tanford (1967)
C-terminus	3.8	Nozaki and Tanford (1967)
N-terminus	7.5	Nozaki and Tanford (1967)
Heme propionate	4.8	Moore and Pettigrew (1990)

In more detail, this program is performing the following steps:

- For each titratable group, the program constructs a model compound, whose pK_a values is experimentally accessible (Table 3.5). This model compound is the titratable group in solution isolated from the remaining molecule, but with the same conformation as in the protein. In the case of amino acids as titratable groups, the model compound is the *N*-formyl *N*-methylamide derivative of the respective amino acid.

- The program calculates $pK_{intr,\mu}$ as a difference to these experimental model compound pK_a values $pK_{mod,\mu}$:

$$pK_{intr,\mu} = pK_{mod,\mu} + \frac{\Delta\Delta G_\mu}{RT \ln 10} \tag{3.2}$$

  $\Delta\Delta G_\mu$ consists of two contributions, the Born energy $\Delta\Delta G_\mu^{Born}$ and the energy of interaction with other charges than those of the titratable group μ, $\Delta\Delta G_\mu^{back}$:

$$\Delta\Delta G_\mu = \Delta\Delta G_\mu^{Born} + \Delta\Delta G_\mu^{back} \tag{3.3}$$

- For each titratable group, the PBE is solved four times, to get the electrostatic potential caused by the charges of the protonated model compound $\phi_\mu^{mod,p}$, of the deprotonated model compound $\phi_\mu^{mod,d}$, of the protonated titratable group within the protein $\phi_\mu^{in,p}$, and of the deprotonated titratable group within the protein $\phi_\mu^{in,d}$.

- $\Delta\Delta G_\mu^{Born}$ and $\Delta\Delta G_\mu^{back}$ are now calculated according to the following equations, where the first sum runs over all atoms m of the titratable group μ with charge q_m^p in the protonated and q_m^d in the unprotonated state, and the second sum runs over all remaining atoms j with charge q_j.

$$\Delta\Delta G_\mu^{Born} = \frac{1}{2}\sum_m q_m^p \left(\phi_\mu^{in,p}(\vec{r}_m) - \phi_\mu^{mod,p}(\vec{r}_m)\right) - q_m^d \left(\phi_\mu^{in,d}(\vec{r}_m) - \phi_\mu^{mod,d}(\vec{r}_m)\right) \tag{3.4}$$

$$\Delta\Delta G_\mu^{back} = \sum_j q_j \left(\phi_\mu^{in,p}(\vec{r}_j) - \phi_\mu^{in,d}(\vec{r}_j) - \phi_\mu^{mod,p}(\vec{r}_j) + \phi_\mu^{mod,d}(\vec{r}_j)\right) \tag{3.5}$$

  The grid artifact, which occurs in eq 3.4 due to the divergent self energy (see section 1.1.2.3), cancels since it is equal in the first and second term of eq 3.4. This is warranted by creating the model compound with the same conformation and the same position relative to the grid as the titratable group in the protein.

- $W_{\mu\nu}$, *i. e.* the electrostatic interaction energy of the titratable groups μ and ν is calculated according to the following equation, where the sum runs over all atoms n of the titratable group ν.

$$W_{\mu\nu} = \sum_n \left(q_n^p - q_n^d\right)\left(\phi_\mu^{in,p}(\vec{r}_n) - \phi_\mu^{in,d}(\vec{r}_n)\right) \tag{3.6}$$

The PBE was solved using a three-step grid-focusing procedure (see section 1.1.2.2) with a starting grid resolution of 2.5 Å, an intermediate grid resolution of 1.0 Å, and a final grid resolution of 0.3 Å. We used an ion exclusion layer of 2 Å, and a solvent probe radius of 1.4 Å. For the solvent, we used a dielectric constant of $\varepsilon = 80$ and a ionic strength of 100 mM. The dielectric constant in the protein was set to $\varepsilon_p = 4$. These parameter values are similar to those used in earlier calculations investigating the protonation of the bRC (Beroza *et al.*, 1995; Lancaster *et al.*, 1996). (For a more extensive discussion see section 3.2.3.5.) We neglected the influence of the membrane, since calculations on the membrane protein bacteriorhodopsin with (Bashford & Gerwert, 1992) and without (Sampogna & Honig, 1994) a membrane model yielded basically the same results. We accounted for the δ and ε tautomers of histidine by considering histidines as double sites as described by Bashford *et al.* (1993).

3.1.2.4 Calculation of protonation probabilities by MC titration

The protonation probability $\langle x_\mu \rangle$ of the group μ can be calculated by evaluating the thermodynamic average over all 2^N possible protonation states n given by eq 3.7,

$$\langle x_\mu \rangle = \frac{\sum_{n=1}^{2^N} x_\mu^n \exp(-G^n/RT)}{\sum_{n=1}^{2^N} \exp(-G^n/RT)} \tag{3.7}$$

This thermodynamic average cannot be calculated exactly in general, since the number of possible protonation states is often far too large(2^N with $N \approx 200$ for the bRC). Instead, we sampled the set of protonation states using a Metropolis Monte Carlo (MC) method (Beroza *et al.*, 1991). This MC method is implemented in the program KARLSBERG (Rabenstein, 1999), which is described in appendix E.

Based on the intrinsic pK_a values, KARLSBERG guesses an initial protonation state vector $\vec{x}$. This should prevent to start with an extremely rare protonation state, which could happen if starting with a random protonation state vector. The elementary MC move is the attempt to change the protonation state of a randomly chosen titratable group with subsequent evaluation of the Metropolis criterion.

This means, KARLSBERG compares the energy before and after the MC move according eq 3.1. If the new energy is lower than the old energy, the move is accepted. Otherwise, it is accepted with probability $\exp(-\Delta G/RT)$.

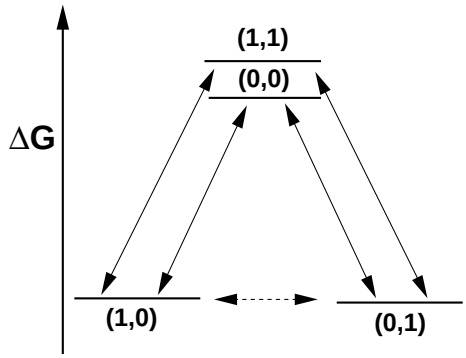

Figure 3.5: Treatment of two strongly coupled sites in Monte Carlo titration calculation. If the energy barrier for the transition from state (1,0) to state (0,1) via the states (1,1) or (0,0) is too large (solid arrows), a Monte Carlo step is performed that simultaneously switches the protonation states of both sites (dashed arrow).

If two groups are strongly coupled, the intermediate state between two protonation states may have a high energy and so the transition from one state to another might be unlikely as depicted in Figure 3.5. The problem can be avoided when the protonation of the two groups are switched simultaneously, which can correspond to a direct proton exchange between these two groups. The double switch is accepted according to the Metropolis criterion. If whole clusters of titratable groups are strongly coupled (which is common if the dielectric constant for the protein is very low as in section 3.2), it might be necessary to apply even triple moves (Rabenstein *et al.*, 1998a). For the bRC, we treated pairs of titratable groups coupled by more than 3 pK_a units by double moves, and triples of titratable groups, where at least two of the possible three pairs are coupled by more than 6 pK_a units, by triple moves (Rabenstein *et al.*, 1998a). A so-called MC scan comprises as many MC steps as titratable single groups, doubles, and triples are available.

To estimate the statistical uncertainty of the MC calculation, it is necessary to calculate the number of independent data sets in the sample (Beroza *et al.*, 1991). The correlation function for the protonation of group μ determines a correlation time τ_μ^{corr} between approximately independent measurements. It is given by

$$C_\mu(\tau) = \frac{1}{T-\tau} \sum_{t=0}^{T-\tau-1} x_\mu(t+\tau)x_\mu(t) - \langle x_\mu \rangle^2 \tag{3.8}$$

where t is the time in units of one MC scan, T is the total number of scans (or the maximum time), and τ is the time variable of the correlation function. The correlation time τ_μ^{corr} is the time for which $C_\mu(\tau)$ becomes negligible (for instance $\mid C_\mu(\tau) \mid < C_\mu(0)/10$). The number of independent measurements is T/τ_μ^{corr}. The variance of one measurement is $C_\mu(0)$. The use of the average of T/τ_μ^{corr} independent measurements provides the standard deviation σ_μ given in eq 3.9.

$$\sigma_\mu = \sqrt{\frac{C_\mu(0)}{T/\tau_\mu^{corr}}} \tag{3.9}$$

The MC sampling for the bRC from *Rps. viridis* was done at pH 7.5, the sampling for the bRC from *Rb. sphaeroides* at pH 7.0. The temperature for both samplings was 300 K. The protonation states of all titratable groups of the bRC from *Rps. viridis* were calculated separately for each of the

ten possible protonation and redox states of the quinone pair (column 1 of Table 3.6). For the bRC from *Rb. sphaeroides*, we considered only the quinone states $Q_A^{\cdot -}Q_B$ and $Q_AQ_B^{\cdot -}$, but calculated both with the dark-adapted as well as with the light-exposed x-ray structure. Arginine, aspartate, cysteine, glutamate, histidine, lysine, tyrosine, and the C- and N-terminus, if not formylated, were considered as titratable groups. The histidines coordinating the magnesium ions of the chlorophylls and also the glutamate and the histidines coordinating the non-heme iron were not considered as titratable groups.

For each MC sampling, we did at first 10 MC scans for equilibration and after that 3000 MC scans as for production. Then we fixed the protonation of all groups whose protonation probability differed from unity or zero by less than 10^{-4} in their respective protonation state and excluded these groups from further MC sampling. With this reduced set of titratable groups, we performed another 7000 MC scans. The sampling was sufficient to reach a standard deviation of less then 0.01 protons at each individual titratable group. In general, the standard deviation of a single group was much smaller than 0.01. The sum of the standard deviations of all protonation probabilities was for each state about 0.02 protons.

3.1.2.5 Energetics of electron transfer and protonation of the quinones

After the calculation of protonation patterns of the bRCs with fixed redox and protonation state of the quinones, we did additional computations where we included also specific redox and protonation reactions of the quinones. Only Q_B was considered to be titratable. We calculated the following protonation reactions for the bRC from *Rps. viridis*: $Q_A^{\cdot -}Q_B^{\cdot -} \rightarrow Q_A^{\cdot -}Q_BH_{dist}$, $Q_A^{\cdot -}Q_B^{\cdot -} \rightarrow Q_A^{\cdot -}Q_BH_{prox}$, $Q_AQ_BH_{dist}^- \rightarrow Q_AQ_BH_2$, $Q_AQ_BH_{prox}^- \rightarrow Q_AQ_BH_2$. We did this by simply including Q_B as an additional titratable group. As model compound for Q_B we used the unmodified UQ in aqueous solution. However, UQ is not soluble in pure water, so that the experimental pK_a value is not directly accessible. Swallow (1982) and Morrison *et al.* (1982) extrapolated the pK_a values of the quinones from pK_a values of water soluble quinone derivatives taking into account the effect of different quinone ring substituents on the pK_a value. The resulting pK_a values are 4.9 for $UQ^{\cdot -}/UQ^{\cdot}H$ and 11.7 for UQH^-/UQH_2.

For the redox reactions, we treated the quinones as redox-active compounds. In principle, a redox-active group can be treated in the same way as a titratable group. The titratable group depends on pH value, which is replaced by the solution redox potential for a redox-active group (Ullmann & Knapp, 1999; Ullmann, 2000). Here, we consider the two quinones as one extended redox-active group with two possible redox states for each calculated redox reaction, which are the first electron transfer with the initial state $Q_A^{\cdot -}Q_B$ and the final state $Q_AQ_B^{\cdot -}$, and the second electron transfer to the unprotonated Q_B with the the initial state $Q_A^{\cdot -}Q_B^{\cdot -}$ and the final state $Q_AQ_B^{2-}$. The first electron transfer was investigated for all bRCs, *i. e.* the bRC from *Rps. viridis* and the light-exposed and dark-adapted bRC from *Rb. sphaeroides*. The second electron transfer was only investigated for the bRC from *Rps. viridis*. The transition between these two states does not depend on the solution redox potential since it corresponds to an internal electron transfer. This transition was included in the move set of the MC sampling.

The model compound for the redox reactions is the couple of quinones in aqueous solution. As experimental "pK_a" value the difference of redox potential in aqueous solution is needed. However, redox potentials of quinones cannot be measured in a protic solvent, since a reduced quinone will inevitably take up a proton. Redox potentials in aprotic solvents, however, are known; $MQ/MQ^{\cdot -}$ in DMF (dimethylformamide): -709 mV, $UQ/UQ^{\cdot -}$ in DMF: -602 mV (Prince *et al.*, 1983), and $UQ^{\cdot -}/UQ^{2-}$ in acetonitrile: -1450 mV (Morrison *et al.*, 1982). We corrected the redox potentials of the quinones obtained in non-aqueous solutions to get redox potentials in aqueous solutions by accounting for the different solvation energies in the respective solvents. For that purpose, we calculated the energy for dissolving the quinones in their different redox states in water, acetonitrile, and

DMF by the continuum electrostatic method (Sitkoff *et al.*, 1994). In the calculations, the following solvent parameters were used: The dielectric constants are $\varepsilon = 80$ for water, $\varepsilon = 38$ for acetonitrile, and $\varepsilon = 37$ for DMF (Lide, 1992). The solvent radii are 1.4 Å for water, 2,0 Å for acetonitrile, and 2.8 Å for DMF. Finally we obtained the following redox potentials of the quinones in aqueous solution: -699 mV for $MQ/MQ^{\cdot -}$, -592 mV for $UQ/UQ^{\cdot -}$, and -1420 mV for $UQ^{\cdot -}/UQ^{2-}$.

After MC sampling, we calculated the free energy difference of the initial and final state of a certain redox or protonation reaction by the following equation:

$$\Delta G = -k_B T \ln \frac{\langle x \rangle}{1 - \langle x \rangle} \tag{3.10}$$

where $\langle x \rangle$ and $1 - \langle x \rangle$ are the average occupancies of the final and initial state, respectively.

If the free energy difference ΔG is not close to zero, the probability $\langle x \rangle$ is close to zero or unity and thus even a small statistical error of the MC sampling leads to a large statistical error of ΔG . To solve this problem, we applied a bias to the sampling of the two redox states (Beroza *et al.*, 1995). We chose the bias iteratively such that the probability $\langle x \rangle$ reached a value close to 0.5, which minimized the statistical error of the calculated energy. At the end, the bias was removed from the calculated values to get the original result, but with a strongly reduced statistical error.

3.1.3 Results and Discussion

3.1.3.1 Total protonation and protonation patterns

Review of experimental results. Proton uptake by wild type and mutant bRCs during electron-transfer and protonation reactions of the quinones was studied experimentally by several research groups (Maróti & Wraight, 1988; McPherson *et al.*, 1988, 1993; Sebban *et al.*, 1995; Brzezinski *et al.*, 1997; Miksovska *et al.*, 1999). According to some experiments measuring directly the proton uptake (McPherson *et al.*, 1988; Brzezinski *et al.*, 1997), the proton uptake of the whole bRC due to the electron transfer from $Q_A^{\cdot -}$ to Q_B at pH 7.0 is close to zero. Also the pH independence of the electron transfer energy in the pH range between 6 and 8.5 (Kleinfeld *et al.*, 1984a) implies no proton uptake. Other measurements of proton uptake, however, suggest an uptake of about 0.5 protons (Miksovska *et al.*, 1999; Maróti & Wraight, 1988) upon electron transfer from Q_A to Q_B.

Also the protonation behavior of individual titratable groups is controversial. On one hand there are several FTIR studies suggesting that no significant proton uptake of carboxylic groups occurs upon Q_B^- formation in the bRC from *Rb. sphaeroides* (Hienerwadel *et al.*, 1995; Nabedryk *et al.*, 1995, 1998) as well as from *Rps. viridis* (Breton *et al.*, 1996; Breton & Nabdryk, 1998), with the only exception of Glu-L212 in the bRC from *Rb. sphaeroides*, which takes up 0.3 to 0.4 protons (Hienerwadel *et al.*, 1995; Nabedryk *et al.*, 1995). Especially, Glu-H173 and Asp-L213 were reported not to contribute significantly to proton uptake (Nabedryk *et al.*, 1998). On the other hand there are other studies on wild-type and mutant bRCs from *Rb. sphaeroides*, investigating electron-transfer rates (Paddock *et al.*, 1997) and the pH dependent proton uptake (Paddock *et al.*, 1989; Takahashi & Wraight, 1992) and electrogenic events (Brzezinski *et al.*, 1997) upon Q_B^- formation. The measurements of pH dependent proton uptake (Paddock *et al.*, 1989; Takahashi & Wraight, 1992) and electrogenic events (Brzezinski *et al.*, 1997) for the bRC from *Rb. sphaeroides* assign a pK value of about 9.5 to Glu-L212, resulting in an essentially protonated Glu-L212 at neutral pH, which does not change its protonation state. Mutation studies imply no participation of Glu-L212 in proton uptake at pH 7.5 and below (McPherson *et al.*, 1994; Miksovska *et al.*, 1996). The discrepancy between these results and the FTIR studies may be resolved by assuming a non-classical titration behavior of Glu-L212 (Brzezinski *et al.*, 1997). This assumption is reasonable, because Glu-L212 is part of a strongly coupled cluster of titratable groups. However, the study of Paddock *et al.* (1997) suggests that also at pH 7.5 Glu-L212 is always protonated and Asp-L213 is a more probable candidate for

proton uptake. The reason for this contradiction may be the uncertainties in interpreting experimental results. Especially the common assignment of measured results to certain residues by mutation studies may be wrong if the mutation causes unexpected conformational and electrostatic effects in the bRC. For the FTIR studies, another explanation was suggested on the basis of observed IR signatures for highly polarizable hydrogen-bond networks suggesting that the protons taken up upon quinone reduction tend to reside more on the bound water molecules of the network than on carboxylic groups themselves, which would make them invisible for FTIR measurements (Breton & Nabdryk, 1998; Breton *et al.*, 1999).

Computational results. Using a continuum electrostatic method, we calculated the protonation patterns and the total protonation of the bRC from *Rps. viridis* for all possible states of the quinones as shown in Figure 3.6 (page 49). For the quinone states $Q_A^{\cdot -}Q_B$ and $Q_AQ_B^{\cdot -}$, we also calculated the protonation patterns and the total protonation of the light-exposed and dark-adapted bRC structure from *Rb. sphaeroides*. In contrast to theoretical studies by other groups (Beroza *et al.*, 1995; Lancaster *et al.*, 1996; Grafton & Wheeler, 1999; Alexov & Gunner, 1999), we considered not only those bRC states in which the quinones are in different redox states, but also those bRC states in which Q_B is protonated. For the bRC from *Rps. viridis*, Table 3.6 shows the protonation probability

Table 3.6: Total protonation and some single-site protonations at pH 7.5. All residues within a distance of 25 Å from the quinones and with at least 0.05 protons deviation from standard protonation are shown, except N-termini of L- and M-chain which are completely deprotonated in all states. Histidines protonated only at N_ε are considered to be in standard protonation and therefore are not included in the table.

state of quinones	histidine (tautomers)[1]				glutamate					total[2]		
	L211		M16		H45	H177	H234	L104	L212	this calculation	experimental values	other calculations
	δ	ε	δ	ε								
Q_AQ_B	0.47	0.53	0.25	0.73	0.05	0.03	0.27	1.00	0.99	0.00	0.00	0.00
$Q_A^{\cdot -}Q_B$	0.50	0.50	0.25	0.72	0.06	0.06	0.30	1.00	0.99	0.14	0.24[5] / 0.34[6,7]	0.5[3,4]
$Q_AQ_B^{\cdot -}$	0.53	0.47	0.25	0.73	0.05	0.59	0.26	1.00	1.00	0.60	0.37[7] / 0,90[6]	0.7[3] / 0.5[4]
$Q_A^{\cdot -}Q_B^{\cdot -}$	0.53	0.47	0.25	0.73	0.06	0.80	0.27	1.00	1.00	0.88		
$Q_A^{\cdot -}Q_BH_{dist}$	0.48	0.52	0.25	0.73	0.06	0.05	0.31	1.00	1.00	1.15		
$Q_A^{\cdot -}Q_BH_{prox}$	0.48	0.52	0.25	0.73	0.06	0.07	0.30	1.00	0.98	1.14		
$Q_AQ_B^{2-}$	0.58	0.42	0.24	0.74	0.05	0.99	0.25	1.00	1.00	0.97		2.6[4]
$Q_AQ_BH_{dist}^-$	0.54	0.46	0.25	0.73	0.05	0.68	0.25	1.00	1.00	1.68	1.3[9]	
$Q_AQ_BH_{prox}^-$	0.52	0.48	0.24	0.74	0.05	0.65	0.25	1.00	1.00	1.65		
$Q_AQ_BH_2$	0.46	0.54	0.24	0.73	0.05	0.03	0.28	1.00	0.99	2.01	1.9[8] / 2.1[9]	

[1] remaining part is protonated at $N_{\delta 1}$ and $N_{\varepsilon 2}$
[2] expressed as difference to the ground state
[3] *Rb. sphaeroides*, ref. (Beroza *et al.*, 1995)
[4] *Rps. viridis*, ref. (Lancaster *et al.*, 1996)
[5] *Rb. capsulatus*, ref. (Sebban *et al.*, 1995)
[6] *Rb. sphaeroides*, ref. (Maróti & Wraight, 1988)
[7] *Rb. sphaeroides*, ref. (McPherson *et al.*, 1988)
[8] *Rb. sphaeroides*, ref. (McPherson *et al.*, 1993)
[9] *Rb. sphaeroides* Glu-L212→Gln mutant, ref. (McPherson *et al.*, 1994)

of non-standard protonated residues that are less than 25 Å away from the quinones. Furthermore, the difference between the total protonation of the ground state Q_AQ_B of the bRC and the total protonation of the respective other states are listed in comparison to previous experimental and theoretical values. Our results imply that the proton uptake by the bRC occurs predominantly during the redox reactions of the quinones, whereas the proton uptake by the bRC coupled to the protonation of Q_B is smaller. An uptake of about 0.2 protons on average goes along with each of the two reductions of Q_A

(Figure 3.6 on page 49). With exception of the electron transfer to the singly reduced, unprotonated Q_B, all electron transfers from Q_A to Q_B (Figure 3.6) are coupled to an uptake of about 0.5 protons on average. The protonation of Q_B in the states $Q_A^{\cdot-}Q_B^{\cdot-}$, $Q_AQ_BH^-_{dist}$, and $Q_AQ_BH^-_{prox}$ induces an uptake of only about 0.3 protons on average (Figure 3.6). This means that an excess proton is already partially available in the protein matrix, before the protonation of Q_B actually occurs.

Our changes of the total protonation calculated for the bRC from *Rps. viridis* are in reasonable agreement with the experimental results. However, the measured value of proton uptake depends sensitively on details of the experimental procedure, so that different groups got significantly different results (Table 3.6). Discrepancies between experiments and calculations may be explained by the fact that most experimental values are obtained from bRCs of purple bacteria other than *Rps. viridis.* However, we did also calculations with the bRC from *Rb. sphaeroides.* These results will be discussed in the next paragraph. Another possible reason for general discrepancies between experimental and calculated values is that experimental values cannot easily be assigned to a specific bRC state, since often only the redox state and not the protonation state of the quinones is determined by experimental conditions. We assigned the experimental values of protonation changes to the states that are, according to our calculated energies (see below), occupied with the highest probability.

According to our computations, also the bRC from *Rb. sphaeroides* takes up substoichiometrical amounts of protons upon electron transfer from $Q_A^{\cdot-}$ to Q_B: 0.33 protons in the light-exposed x-ray structure and 0.15 protons in the dark-adapted x-ray structure (Table 3.7). The total proton uptake of the dark-adapted x-ray structure is not relevant, because electron transfer will not occur in this structure (see below). The total proton uptake of the light-exposed x-ray structure is in reasonable agreement with the experiments that suggest such a proton uptake (Miksovska *et al.*, 1999; Maróti & Wraight, 1988), but does not support the experiments that did not find any proton uptake (McPherson *et al.*, 1988; Brzezinski *et al.*, 1997). The proton uptake of the bRC due to the electron transfer from $Q_A^{\cdot-}$ to Q_B is determined experimentally by comparing the proton uptake of the native bRC and of a bRC where electron transfer from $Q_A^{\cdot-}$ to Q_B is blocked. In both cases, the bRCs are excited by a single flash from the ground state to the state $P^+Q_AQ_B^{\cdot-}$ and $P^+Q_A^{\cdot-}Q_B$, respectively. The blocking is usually accomplished by replacing Q_B by a redox inactive compound like terbutryn. This replacement may, however, significantly change the protonation behavior of the bRC upon reduction of Q_A, since the Q_A reduction also affects the environment of Q_B (Miksovska *et al.*, 1999). In addition, the transition from the electron-transfer inactive to the active conformation consists mainly of the movement of Q_B from the distal to the proximal binding site. Since Q_B is exchanged by a different compound, the characteristics of the conformational transition, which is anyway strongly dependent on the experimental conditions, will be modified. Our results show a significantly different protonation behavior for the dark-adapted and light-exposed x-ray structures (see also below). Hence, an explanation for the different experimental results may be a modification of the conformational transition and thus of the protonation behavior, depending on the compound used for blocking the electron transfer and other experimental details.

Several titratable groups contribute to the proton uptake by the whole bRC, but most of them participate only with very small protonation changes. Besides the Q_B, the residue Glu-H177 has the largest contribution to the proton uptake in the case of *Rps. viridis* (Table 3.6). The distance of the carboxyl oxygen atom of this residue to the distal oxygen atom of Q_B is 8.0 Å (Figure 3.2). Glu-H177 is possibly also involved in the proton transfer pathway from the solvent to Q_B (Lancaster *et al.*, 1995). According to our calculations, Glu-L212 does not contribute significantly to the proton uptake at pH 7.5, since it is nearly protonated for all redox and protonation states of Q_A and Q_B. However, the very small, but not vanishing ionization probability of Glu-L212 of one to two percent in the states in which Q_B is neutral, shows that Glu L212 just starts to titrate at pH 7.5. The statistical uncertainty of the protonation probability of Glu-L212 is less than 10^{-3} protons in our computation.

In Table 3.7, the protonation probabilities of the aspartates L210 and L213 and of the glutamate

Table 3.7: Summary of the computed results at pH 7.0 for the dark-adapted and light-exposed x-ray structures of the bRC from *Rb. sphaeroides*. Shown are the energies for the electron transfer from $Q_A^{\cdot -}$ to Q_B and the protonation probabilities for selected titratable residues in the fixed redox states $Q_A^{\cdot -}Q_B$ and $Q_AQ_B^{\cdot -}$ and in the equilibrium distribution between the two states. L210 and L213 are aspartates, L212 is a glutamate. The standard deviation of the single-site protonation probabilities is smaller than 0.001 protons.

			protonation probabilities								
	$Q_A^{\cdot -}Q_B \rightarrow Q_AQ_B^{\cdot -}$		$Q_A^{\cdot -}Q_B$			$Q_AQ_B^{\cdot -}$			equilibrium		
structure	energy	proton uptake	L210	L212	L213	L210	L212	L213	L210	L212	L213
dark (`1aij`)	+157 meV	0.15±0.03	0.01	0.27	0.75	0.01	0.60	0.85	0.01	0.27	0.75
light (`1aig`)	-56 meV	0.33±0.02	0.02	0.81	0.37	0.00	1.00	0.99	0.00	0.98	0.93

L212 in the bRC from *Rb. sphaeroides* are shown. Glu-L212 and Asp-L213 are the only groups with non-standard protonation probability within a distance of 10 Å from Q_B (see also Figure 3.2 on page 34). In contrast to *Rps. viridis*, not Glu-H173 (which is the equivalent of Glu-H177 in *Rps. viridis*), but Glu-L212 (also Glu-L212 in *Rps. viridis*) and Asp-L213 (which is a non-titratable Asn L213 in *Rps. viridis*) are the only residues with a large protonation change upon the first electron transfer. The residues Asp-L210 (Glu-L210 in *Rps. viridis*), Glu-L212, Asp-L213 (not available as titratable residue in *Rps. viridis*) and Glu-H173 (Glu-H177 in *Rps. viridis*) constitute a strongly coupled cluster of titratable groups in close proximity to Q_B. The protonation pattern of such a coupled cluster can be altered dramatically by small energy changes, if the p*K* values of the individual titratable groups are not too different and no net protonation or deprotonation of the whole cluster occurs. This effect has to be kept in mind for the following discussion of the detailed distribution of protons within the cluster. The proton uptake of the coupled cluster is for both, the light-exposed and dark-adapted x-ray structures, more than twice as large than the total proton uptake of the whole bRC from *Rb. sphaeroides*. Hence, more than half of the proton uptake of the cluster is compensated by numerous small protonation changes in the network of titratable groups farther away from Q_B.

The equilibrium between the redox states $Q_A^{\cdot -}Q_B$ and $Q_AQ_B^{\cdot -}$ is for the dark-adapted x-ray structure strongly inclined to the state $Q_A^{\cdot -}Q_B$ and for the light-exposed x-ray structure to the state $Q_AQ_B^{\cdot -}$ (see below). Hence, the entries in the column *equilibrium* of Table 3.7 are similar to those of the $Q_A^{\cdot -}Q_B$ state for the dark-adapted x-ray structure and similar to those of the $Q_AQ_B^{\cdot -}$ state for the light-exposed x-ray structure. When the electron transfer reaction between $Q_A^{\cdot -}$ and Q_B is equilibrated, the cluster of the four strongly coupled residues Glu-H173, Asp-L210, Glu-L212, and Asp-L213 contains two protons in the light structure, but only one proton in the dark structure.

The striking difference of the protonation behavior of Glu-L212 in the bRC from *Rb. sphaeroides* and *Rps. viridis* is in agreement with the experimental findings from FTIR studies (Hienerwadel *et al.*, 1995; Nabedryk *et al.*, 1995, 1998; Breton *et al.*, 1996; Breton & Nabdryk, 1998). However, the protonation changes at Glu-H177 (*Rps. viridis*) and Asp-L213 (*Rb. sphaeroides*) do not agree with the FTIR experiments: If the protonation of Glu-L212 and Asp-L213 in the bRC from *Rb. sphaeroides* is compared in the states $Q_A^{\cdot -}Q_B$ and $Q_AQ_B^{\cdot -}$ for the light-exposed x-ray structure, Asp-L213 takes up 0.5 protons and Glu-L212 is mostly protonated in both states with a take-up of only 0.2 protons. These results are not in agreement with the FTIR results, but they are in agreement with several non-FTIR results (Paddock *et al.*, 1997, 1989; Takahashi & Wraight, 1992; Brzezinski *et al.*, 1997). However, if the state $Q_A^{\cdot -}Q_B$ for the dark-adapted x-ray structure is compared with the state $Q_AQ_B^{\cdot -}$ for the light-exposed x-ray structure, which means that the conformational transition of the conformational gating (see below) is included in the comparison, Glu-L212 takes up 0.7 protons and now Asp-L213 is mostly protonated in both states with a take-up of only 0.2 protons. These results are more in agreement with the FTIR results (Hienerwadel *et al.*, 1995; Nabedryk *et al.*, 1995, 1998). Besides the already

discussed possible reasons for the described contradictions (see above), now another explanation comes into mind. It seems to be critical for the experimental result whether under certain experimental conditions the measurement includes or excludes the conformational transition between dark-adapted and light-exposed x-ray structure. So it may be rewarding to further investigate the events that trigger the conformational transition (Graige *et al.*, 1998).

The x-ray structure of the bRC from *Rps. viridis* is equivalent to the light-exposed x-ray structure of the bRC from *Rb. sphaeroides.* We do not know whether a conformational transition similar to that from the dark-adapted to the light exposed x-ray structure of the bRC from *Rb. sphaeroides* exists also for the bRC from *Rps. viridis.* The calculated take-up of 0.5 protons by Glu-H177 upon $Q_B^{\cdot -}$ formation does not agree with the FTIR results (Breton *et al.*, 1996; Breton & Nabdryk, 1998). As explained above, it might also here be possible that for a highly polarizable hydrogen-bond network involving Glu-L212 and Glu-H177, protons reside in part also at bound water molecules, which could make them invisible for FTIR measurements concentrating on the carboxylic groups (Breton & Nabdryk, 1998; Breton *et al.*, 1999).

Comparison to earlier computations. In a recent molecular dynamics study also based on the dark-adapted and light-exposed x-ray structures from *Rb. sphaeroides* (Stowell *et al.*, 1997), A. K. Grafton and R. A. Wheeler investigated the protonation states of Glu-L212 and Asp-L213 (Grafton & Wheeler, 1999). They found in agreement with our own results that $Q_B^{\cdot -}$ binding at the proximal binding site is only possible when both residues are protonated, whereas binding of the neutral Q_B at the distal site is most consistent with one residue protonated and the other unprotonated. In agreement with non-FTIR experimental results (Paddock *et al.*, 1997), they propose that the proton binds preferentially at Glu-L212 and not at Asp-L213.

The most significant difference in protonation patterns between this work and a study on the bRC from *Rb. sphaeroides* by Alexov and Gunner (1999) is the protonation of Glu-L212 and Asp-L210. While we calculated a protonation change of Glu-L212 of 0.2 to 0.7 (depending on including the conformational transition or not) in reasonable agreement with FTIR results (Hienerwadel *et al.*, 1995; Nabedryk *et al.*, 1995, 1998), Alexov and Gunner (1999) found Glu-L212 to be always protonated. According to Alexov and Gunner (1999), a large protonation change is localized at Asp-L210, which is always nearly unprotonated in our study.

Also a study on the bRC from *Rps. viridis* by Lancaster *et al.* (1996) applied similar methods as the present one. This study shows protonation changes localized at the residues Glu-H177, Glu-L212, and Glu-M234. The protonation change of carboxylic groups is in contradiction with the FTIR experiments that suggest no proton uptake of carboxylic groups at all (Breton *et al.*, 1996; Breton & Nabdryk, 1998). However, the reported protonation changes are all small (0.15 protons per titratable group or less). In our own study (Rabenstein *et al.*, 1998b), Glu-L212 is in agreement with the experiments always protonated, but the change of protonation is mainly localized at Glu-H177 (see above).

3.1.3.2 First Electron Transfer from Q_A to Q_B.

Review of experimental results. The experimental values of the electron-transfer energy are determined by measuring the recombination rates of the bRC states $P^+Q_A^{\cdot -}Q_B$ and $P^+Q_AQ_B^{\cdot -}$ to the ground state PQ_AQ_B. For the $P^+Q_AQ_B^{\cdot -}$ decay, direct recombination is negligible (Kleinfeld *et al.*, 1982; Wraight, 1979; Wraight & Stein, 1980). Instead, it is assumed that the state $P^+Q_AQ_B^{\cdot -}$ is in equilibrium with the state $P^+Q_A^{\cdot -}Q_B$ and recombination occurs nearly exclusively from $P^+Q_A^{\cdot -}Q_B$ (Figure 3.7 on page 54). Therefore, if the equilibrium between the states $Q_A^{\cdot -}Q_B$ and $Q_AQ_B^{\cdot -}$ is reached fast compared to the recombination rate from $P^+Q_A^{\cdot -}Q_B$ to the ground state, the equilibrium constant K_{AB} can be calculated from the measured recombination rates with the following equation (Mancino *et al.*,

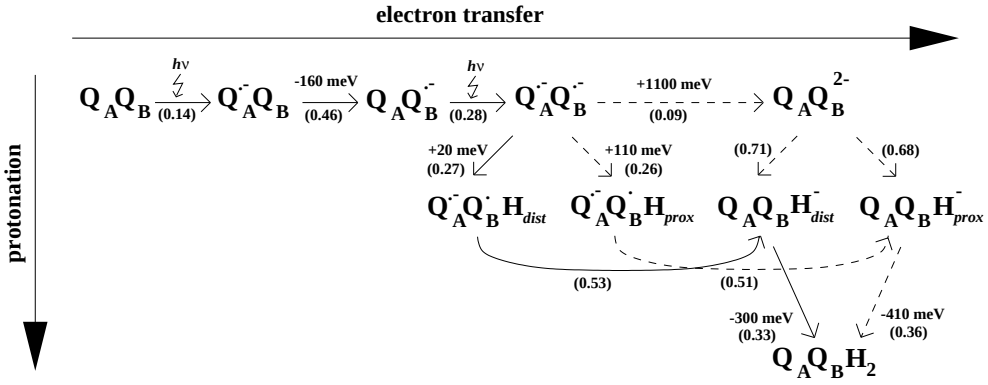

Figure 3.6: Scheme of the possible electron-transfer and protonation reactions involving the quinones of the bRC. Solid arrows are used for the energetically preferred reaction sequence. Calculated reaction energies are given near the respective arrows. Changes in total protonation during the reactions are given in parentheses. All results are calculated for *Rps. viridis*.

1984; Kleinfeld *et al.*, 1984a; Tandori *et al.*, 1999):

$$K_{\mathrm{AB}} = \frac{k_{\mathrm{AP}}}{k_{\mathrm{BP}}} - 1 \tag{3.11}$$

k_{AP} is the recombination rate from the state $\mathrm{P^+Q_A^-Q_B}$, measured in a bRC where electron transfer to $\mathrm{Q_B}$ is blocked. k_{BP} is the effective recombination rate from the state $\mathrm{P^+Q_AQ_B^-}$. From the equilibrium constant K_{AB}, the reaction energy of the electron transfer from $\mathrm{Q_A^-}$ to $\mathrm{Q_B}$ can be calculated similar as in eq 3.10. By this method, the electron-transfer energy was determined by different groups to be -78 meV at pH 7.8 (Arata & Parson, 1981), -71 meV at pH 8.0 (Mancino *et al.*, 1984), nearly constant -67 meV from pH 6.0 to 8.5 (Kleinfeld *et al.*, 1984a), or -52 meV at pH 8.1 (Tandori *et al.*, 1999) for *Rb. sphaeroides* and -175 meV at pH 6.0 (Baciou *et al.*, 1991), -150 meV at pH 7.5 and 9.0 (Baciou *et al.*, 1991), or -120 meV at pH 9.0 (Shopes & Wraight, 1985) for *Rps. viridis.*

Computational results. For the reaction energy of the electron transfer from $\mathrm{Q_A^-}$ to $\mathrm{Q_B}$ our continuum electrostatic calculations yielded an energy difference of -160 meV at pH 7.5 for *Rps. viridis* (Figure 3.6). We computed a value of -56 meV for the light-exposed x-ray structure and a value of +157 meV for the dark-adapted x-ray structure of the bRC from *Rb. sphaeroides* (both at pH 7.0, see Table 3.7 on page 47). Assuming that the electron transfer in the bRC from *Rb. sphaeroides* occurs exclusively in a conformation corresponding to the light-exposed x-ray structure (for discussion of this topic see next paragraph and section 3.1.3.6), our calculated values are in excellent agreement with experimental findings.

According to our computation, the electron transfer is energetically uphill in the dark-adapted x-ray structure and downhill in the light-exposed x-ray structure of the bRC from *Rb. sphaeroides*. From a thermodynamic point of view, we can therefore support the assumption that the dark-adapted x-ray structure represents the electron-transfer inactive conformation of the bRC and the light-exposed x-ray structure the electron-transfer active conformation. The implication of this finding for the conformational gating mechanism is discussed in section 3.1.3.6. The calculated value for the light-exposed x-ray structure being in agreement with experimentally determined values implies that the bRC adopts completely the electron-transfer active conformation in both states $\mathrm{Q_A^-Q_B}$ and $\mathrm{Q_AQ_B^-}$, since we have exclusively considered the light-exposed x-ray structure, which is assumed to represent the electron-transfer active conformation. In reality, both states may consist of a mixture of electron-transfer active and inactive conformations as denoted in Figure 3.7 on page 54. The possible influence of the

distribution of electron-transfer active and inactive conformations on the experimentally determined electron-transfer energy is also discussed in the section 3.1.3.6.

Comparison to earlier computations. The energetics of the electron transfer from $Q_A^{\cdot -}$ to Q_B in the bRC from *Rb. sphaeroides* and *Rps. viridis* was investigated several times by electrostatic approaches similar to that used in the present work. The first of these studies was done by Beroza *et al.* (1995) on the bRC from *Rb. sphaeroides*. However, they failed to reproduce the experimental value of the electron-transfer energy. The electron transfer was calculated to be uphill by 170 meV. Three years later, we started our own studies on the bRC from *Rps. viridis*, the first without conformational flexibility (Rabenstein *et al.*, 1998b), which is reported here, and the second with conformational relaxation (Rabenstein *et al.*, 1998a), which is reported in section 3.2. The study on the bRC from *Rb. sphaeroides* followed in 2000 (Rabenstein *et al.*, 2000). In all three studies, we could reproduce the experimental value of the electron-transfer energy faithfully (see also section 3.2). Recently, Alexov and Gunner (1999) studied the electron transfer from $Q_A^{\cdot -}$ to Q_B also based on the light-exposed and dark-adapted x-ray structures (Stowell *et al.*, 1997) as we did it in the present study. Alexov and Gunner (1999) took the backbone conformation from the dark-adapted x-ray structure. They generated the side-chain conformers and the binding position of Q_B according to both, the dark-adapted and the light-exposed structures, and several additional bRC structures from *Rb. sphaeroides* and *Rps. viridis.* They included also different conformers of polar hydrogens that are part of a titratable group. The possible combination of conformers were sampled using a generalized MC method (Beroza & Case, 1996; Alexov & Gunner, 1997) described in more detail in section 4.2.1. In their calculation, also explicit water molecules were included in different orientations, which were also sampled by the MC method. By this method, they included conformational flexibility in their calculations and could reproduce the experimental value for the electron-transfer energy. However, without conformational flexibility, they calculated the electron transfer to be uphill by 165 meV. They report similar results of R. Lancaster and M. R. Gunner for the bRC from *Rps. viridis* (unpublished results cited in Alexov and Gunner (1999)).

It is obvious to ask why our own studies reproduce the experimental energy value successfully and all other studies failed. In the past, we proposed as the main reason for our success our detailed charge model for the cofactors of the bRC derived from quantum-chemical calculations. In particular, the charges for the non-heme iron center and the quinone in their different redox states (Rabenstein *et al.*, 1998b, 1998a) differ significantly from those of the simplified charge model used in the other studies (Beroza *et al.*, 1995; Lancaster *et al.*, 1996; Alexov & Gunner, 1999). Alexov and Gunner (1999) question that assumption and emphasize the fact that the past studies all used different bRC structures. Without doubt, even moderate conformational changes can have a large effect on electrostatic energies (Rabenstein *et al.*, 1998a). R. Lancaster and M. R. Gunner used for their calculation of the electron transfer energy in the bRC from *Rps. viridis* (unpublished results cited in Alexov and Gunner (1999)) a new x-ray structure with a better defined Q_B binding site (Lancaster and Michel (1997, 1999), PDB code 2prc), which was, however, not publicly available at the time we did our studies. To use the improvements of the new structure anyhow, we applied two well defined modifications (Rabenstein *et al.*, 1998b) to an older x-ray structure (Deisenhofer *et al.* (1995), PDB code 1prc) according to information already published at that time (Lancaster & Michel, 1996; Lancaster *et al.*, 1995). By this way, the structure we used for our studies (Rabenstein *et al.*, 1998b, 1998a) was very similar to that used by R. Lancaster and M. R. Gunner. As soon as the new x-ray structure (Lancaster & Michel, 1997, 1999) was publicly available, we repeated our calculation using this structure, which resulted in an electron-transfer energy of -169 meV compared to -160 meV as calculated with our modified structure. Hence, for the bRC from *Rps. viridis*, the structural differences cannot explain the differences in the computational results. However, for the studies on the bRC from *Rb. sphaeroides*, structural differences may be more significant. Beroza *et al.* (1995) used another structure (PDB

code 4rcr) than Alexov and Gunner (1999) and us in the present work. Although the latter two studies are based on the same x-ray structures (Stowell *et al.*, 1997), the actually used structures differ. We placed polar hydrogens using the HBUILD facility of the program CHARMM (Brooks *et al.*, 1983) with a subsequent energy minimization (Rabenstein *et al.*, 1998b). E. G. Alexov and M. R. Gunner used the program PROTEUS (Gunner *et al.*, 1996) to place polar hydrogens. We used the original light-exposed and dark-adapted x-ray structure, whereas E. G. Alexov and M. R. Gunner used for their calculation with a single protein conformation the backbone from the dark structure, which is, however, nearly identical to the backbone of the light structure. They selected for each sidechain and for Q_B the conformer with the highest population from their calculations with conformational flexibility for the ground state of the quinones (Q_AQ_B). This selection procedure leads to a structure that will be energetically optimized for uncharged quinones and may prefer one of the two states $Q_A^{\cdot-}Q_B$ and $Q_AQ_B^{\cdot-}$ more than the other.

To probe our assumption that the different charge models are the most important reason for the different results, we repeated our calculation using the charge model used by Lancaster *et al.* (1996) and Alexov and Gunner (1999) for the quinones, resulting in an electron-transfer energy of -6 meV, thus an increase of the electron transfer energy by 50 meV. This is a significant shift but can only partially explain the difference between the calculated energy reported in this work and the energy calculated for the rigid case in the work of Alexov and Gunner (1999). However, the charges of the polypeptides are also different in all three studies and may cause additional significant differences in the electrostatic energy. We used the charges from the CHARMM parameter set provided by Molecular Simulations Inc., which closely resemble those of the CHARMM 19 parameter set (Brooks *et al.*, 1983) but are also available for several amino acids in non-standard protonation. Lancaster *et al.* (1996) and Alexov and Gunner (1999) used PARSE charges (Sitkoff *et al.*, 1994), which tend to be more localized and to have larger absolute values than the CHARMM charges we used. Beroza *et al.* (1995) used charges from the DISCOVER force field (Hagler *et al.*, 1974).

In addition to different charge models and different structures, there are a number of other possible differences in the conditions and techniques of solving the PBE. Most evident is the resolution of the employed grid. We used a grid with a lattice constant of 0.3 Å, whereas Alexov and Gunner (1999) used a relatively coarse grid with a lattice constant of 0.83 Å. Also the inclusion of explicit water molecules can have a significant effect. Alexov and Gunner (1999) included explicit water molecules in their calculation with conformational flexibility. This is reasonable since the water molecules can adopt different orientations in such a calculation. In a calculation with a rigid conformation, the inclusion of explicit water molecules is dangerous if the correct orientation is unknown or if different conformations can be adopted.. However, it is not clear whether Alexov and Gunner (1999) included explicit water molecules in their calculation for the rigid protein. In their work (Alexov & Gunner, 1999), there are contradicting statements in connection with Figure 9 that “waters were deleted” and “waters are rigid”.

3.1.3.3 Second Electron Transfer from Q_A to Q_B and first protonation of Q_B.

Review of experimental results. Three different reactions may follow the first electron transfer process: (i) the second electron transfer from Q_A to Q_B, (ii) the protonation at the proximal oxygen of Q_B, *i. e.* the oxygen atom pointing towards the non-heme iron, or (iii) the protonation at the distal oxygen of Q_B, *i. e.* the oxygen atom pointing away from the non-heme iron (Figure 3.2 on page 34). Based on experimental results, different models were proposed. McPherson *et al.* (1994) came to the conclusion that the first electron transfer is followed by the second electron transfer, whereupon the two protonations of Q_B occur. In contrast, the kinetic results of Graige *et al.* (1996) fitted best to a model in which the first electron transfer is followed by the first protonation. Subsequently, the second electron transfer occurs as the rate determining step. Another model, fitting the kinetic results

of Graige *et al.* (1996) almost as good, includes a concerted mechanism, in which the second electron and the first proton are transferred to Q_B simultaneously. The model derived from mutation studies of Paddock *et al.* (1990) supports also a reaction sequence in which the first electron transfer from Q_A to Q_B is followed by the first protonation of Q_B, the second electron transfer from Q_A to Q_B, and finally by the second protonation of Q_B. In addition, the model of Paddock *et al.* (1990) proposes that the first protonation occurs at the distal oxygen atom of Q_B and the second proton binds to the proximal oxygen atom.

Computational results. We calculated the reaction energy for the second electron transfer from Q_A to Q_B and also for the first protonation of $Q_B^{\cdot -}$ at the distal and at the proximal oxygen atom (Figure 3.6) (only) for the bRC from *Rps. virids.* The energy difference between the bRC states $Q_A^{\cdot -}Q_B^{\cdot -}$ and $Q_AQ_B^{2-}$ is +1100 meV. This energy difference is even higher than the energy difference between the respective quinone states in aqueous solution (720 meV). Thus, according to our calculations, a doubly reduced, unprotonated Q_B is unlikely to occur in the bRC. The protonation energy of Q_B in the bRC state $Q_A^{\cdot -}Q_B^{\cdot -}$ at pH 7.5 is also positive, but small (Figure 3.6). The protonation at the distal oxygen atom is energetically preferred by 90 meV as compared to a protonation at the proximal oxygen atom. Therefore, we propose that after the first electron transfer from Q_A to Q_B, Q_B gets protonated at the distal oxygen atom. This is in agreement with the model of Paddock *et al.* (1990). However, the difference between the protonation energies at the distal and proximal oxygen atom is small. If the protonation at the proximal oxygen is kinetically preferred it may precede the protonation of the distal oxygen atom.

The energy of +20 meV for the first protonation of Q_B at the distal oxygen atom corresponds to an equilibrium partial protonation of about 30 %. This fraction may be too small to detect the singly protonated Q_B spectroscopically. However in the bRC from *Rb. sphaeroides*, the protonation of the singly reduced Q_B does not change (with an uncertainty of ± 5 %) in the pH-range from 4 to 8 (footnote in Graige *et al.* (1996)). One explanation for this behavior can be that the singly reduced Q_B is protonated less than 5 % over this pH-range. According to our calculations, the singly reduced Q_B has a protonation probability of about 30 % at pH 7.5. This result does not contradict the experimental observation, if the protonation probability of the singly reduced Q_B remains constant at (30 ± 5) % over the pH-range from 4 to 8. This may possibly be rationalized with a special titration behavior of Q_B: Due to strong coupling of Q_B with titratable groups in the protein matrix, a nearly constant protonation probability of the singly reduced Q_B may be maintained over a wide pH-range. The assumption of a nearly unprotonated singly reduced Q_B is not supported by our results. But it should be kept in mind that the experiments were done with the bRC from *Rb. sphaeroides*, while we used the structure of the bRC from *Rps. viridis* in our computation.

We found that the proton uptake by the bRC takes place before Q_B gets protonated. This may be one of the reasons for the experimental finding that the first protonation of Q_B is faster than the second electron transfer from Q_A to Q_B (McPherson *et al.*, 1994). Due to the fast protonation of Q_B, the system reaches the protonation equilibrium after the first electron-transfer process. The second electron is then only transferred if Q_B is protonated. If the protonation of Q_B depends on pH, this mechanism can explain the observed pH dependence of the second electron-transfer rate. This model is similar to the one derived from kinetic studies mentioned above (Graige *et al.*, 1996).

3.1.3.4 Second Protonation of Q_B.

Measurements of the energies for the second protonation of Q_B at pH 9.0 and 9.5 gave $\geq(0\pm20)$ meV and $\geq(28\pm20)$ meV, respectively (McPherson *et al.*, 1994). Assuming a Henderson-Hasselbalch titration behavior, the protonation energy at pH 7.5 is -90 meV. This is in qualitative agreement with our calculated values of -300 meV and -410 meV (Figure 3.6). The discrepancy may be explained by

the uncertainty of extrapolating the energy to lower pH-values. Furthermore, the experiments were done at the bRC from *Rb. sphaeroides*, while we used the bRC from *Rps. viridis*. The results show that the state $Q_AQ_BH^-_{dist}$, in which Q_B is protonated at the distal quinone oxygen, is energetically more stable than the state $Q_AQ_BH^-_{prox}$. Hence, also in the doubly reduced state of Q_B, a protonated distal oxygen is preferred to a protonated proximal oxygen.

3.1.3.5 Sequence of electron-transfer and protonation reactions

As discussed above, the sequence of the electron-transfer and protonation reactions, *i. e.* their temporal order, is not completely resolved experimentally. In particular, it is unclear, if the first protonation of Q_B precedes the second electron transfer from Q_A to Q_B or not. Our calculated reaction energy for the reduction of the singly reduced Q_B to a doubly reduced Q_B is in the bRC even higher than in aqueous solution. The reaction energy is larger than 1 eV. This energy is too large to make this state thermally accessible, thus the doubly reduced Q_B state does not occur in the bRC. Therefore, we conclude that the first protonation of Q_B precedes the second electron transfer between Q_A and Q_B. If the protonation of Q_B depends on pH, this mechanism can also explain the pH dependence of the second electron-transfer step (Graige *et al.*, 1996), because the protonation of Q_B would be a prerequisite for the second electron-transfer step. According to our calculated reaction energies (Figure 3.6 on page 49), we propose the following reaction sequence for the electron-transfer and protonation reactions of the quinones in the bRC: (1) first electron transfer from Q_A to Q_B, (2) first protonation of Q_B (at the distal oxygen close to Ser-L223), (3) second electron transfer from Q_A to Q_B, (4) second protonation of Q_B (at the proximal oxygen close to His-L190). Whether the distal or the proximal quinone oxygen atom gets protonated first is, however, not certain, since the corresponding reaction energies differ not much (Figure 3.6). Although the protonation of the distal oxygen atom is energetically favored, the protonation of the proximal oxygen atom can be faster if a proton is more easily available. However, also experimental data suggest, that the protonation of the distal oxygen atom of Q_B precedes the protonation of the proximal oxygen atom (Paddock *et al.*, 1990). The energetically favored reaction sequence is shown with solid arrows in Figure 3.6. This reaction sequence is in agreement with several models derived from experiments (Graige *et al.*, 1996; Paddock *et al.*, 1990). A mechanism in which the first protonation of Q_B and the second electron transfer occur simultaneously, *i. e.* a concerted mechanism (Graige *et al.*, 1996), would also agree with our calculations.

3.1.3.6 Conformational gating

Review of experimental results. Conformational gating (Davidson, 1996) was proposed for the bRC of *Rb. sphaeroides* on the basis of experiments in which the driving force for the electron transfer from $Q_A^{\cdot-}$ to Q_B was varied (Graige *et al.*, 1998). In these experiments, Q_A was replaced by quinones other than UQ that have different redox potentials. However, the electron-transfer rate from $Q_A^{\cdot-}$ to Q_B was not changed significantly by these replacements. The reaction energy of the electron transfer is relatively small so that the electron-transfer process occurs in the normal regime, where the classical Marcus theory (Marcus, 1956; Marcus & Sutin, 1985) predicts a strong dependency of the electron-transfer rate on the reaction energy. The observed independency of the electron-transfer rate on the reaction energy can be explained by a conformational gating mechanism. According to the conformational gating mechanism, the bRC can adopt two conformations: an electron-transfer active conformation and an electron-transfer inactive conformation (Figure 3.7). The electron transfer from $Q_A^{\cdot-}$ to Q_B will occur nearly exclusively in the electron-transfer active conformation. In the ground state PQ_AQ_B, the bRC is preferentially in the electron-transfer inactive conformation. Hence, a conformational transition is necessary to allow the electron transfer from $Q_A^{\cdot-}$ to Q_B. This transition is the rate determining step.

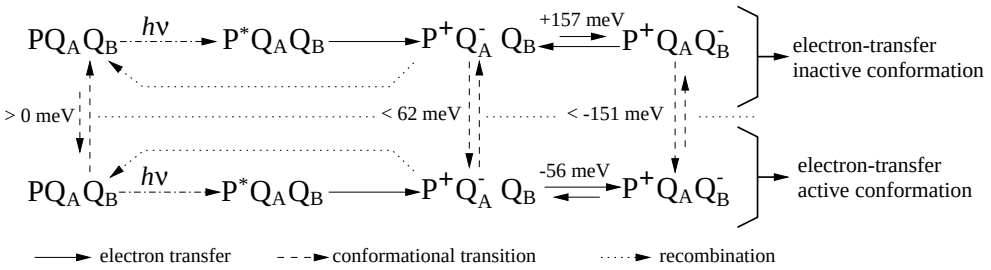

Figure 3.7: Possible electron transfer reactions and conformational gating in the bRC from *Rb. sphaeroides*. The initial reaction is the light excitation of the special pair P to P^*, after which a charge separation follows in the sub-microsecond time regime, resulting in the state $P^+Q_A^-Q_B$. The electron is then transferred from Q_A^- to Q_B in the time scale of several hundred microseconds. According to the conformational gating hypothesis, this process involves a conformational transition, after which the actual electron transfer occurs at a much faster rate. Recombination occurs from the state $P^+Q_A^-Q_B$ to PQ_AQ_B with a time constant of about 100 ms. All states can in principle adopt the two conformations considered in the present study: One where the electron transfer from Q_A^- to Q_B is possible, and one where it is hindered. We assume that the electron-transfer active conformation is represented by the light-exposed x-ray structure and the electron-transfer inactive conformation by the dark-adapted x-ray structure. The hindering of the electron transfer can be mediated kineticly or thermodynamicly (or both). The kinetics is not investigated in the present study, but the thermodynamic result is, that the electron transfer is uphill by 157 meV for the dark-adapted x-ray structure, whereas it is downhill by 56 meV for the light-exposed x-ray structure. Due to the experimental conditions, the bRC was in the ground state PQ_AQ_B for the determination of the dark-adapted x-ray structure and in the charge separated state $P^+Q_AQ_B^-$ for the determination of the light-exposed x-ray structure. Hence, the conformational equilibrium prefers the electron-transfer inactive conformation in the state PQ_AQ_B and the electron-transfer active conformation in the state $P^+Q_AQ_B^-$. The conformational equilibrium constant in the state $P^+Q_A^-Q_B$ is unknown. The upper limit of 62 meV for the conformational transition in the latter state is deduced from comparison of experimental and calculated results (see text for details). The upper limit of -151 meV for the conformational transition in the state $P^+Q_AQ_B^-$ results from the thermodynamic cycle connecting the states $P^+Q_A^-Q_B$ and $P^+Q_AQ_B^-$ in the two conformations.

To determine the two conformations experimentally, x-ray structures were solved of the dark-adapted bRC, which is in the ground state PQ_AQ_B, and of the light-exposed bRC, which was frozen immediately after illumination and therefore in the state $P^+Q_AQ_B^-$ (Stowell *et al.*, 1997). The most striking difference between the two x-ray structures is the displacement of Q_B from a binding site proximal to the non-heme iron to a distal binding site. In the light-exposed x-ray structure, Q_B binds at the proximal binding site, whereas in the dark-adapted x-ray structure it binds at the distal binding site (Figure 3.2 on page 34). However, the electron density at the proximal binding site suggests a partial occupancy of Q_B at the proximal site even in the dark-adapted x-ray structure. It was proposed that the dark-adapted and light-exposed x-ray structures represent the electron-transfer inactive and active conformations, respectively. Thus, in the state $P^+Q_AQ_B^-$ the equilibrium between electron-transfer inactive and active conformations prefers the electron-transfer active conformation, and in the ground state PQ_AQ_B it prefers the electron-transfer inactive conformation. The detected partial occupancy of Q_B at the proximal binding site shows that the preference of the equilibrium for the electron-transfer inactive or active conformation is less pronounced in the ground state than in the state $P^+Q_AQ_B^-$ (Figure 3.7).

This finding is in agreement with kinetic measurements that found the electron transfer rate from Q_A^- to Q_B to be at least biphasic (Tiede *et al.*, 1996; Li *et al.*, 1998). The fast phase can be assigned to the electron transfer in the electron-transfer active conformation, and the slow phase to the conformational transition from the electron-transfer inactive conformation to the electron-transfer active conformation. However, the quantitative results of the two kinetic studies (Tiede *et al.*, 1996; Li *et al.*, 1998) are very different and seem to be highly sensitive to the details of the experimental procedure. The fast rate component of the total reaction yield, which is according to our interpretation identical to the occupancy of the electron-transfer active conformation in the ground state, was measured to be 25 % by Tiede *et al.* (1996) and 60 % by Li *et al.* (1998). A strong preparation dependency was explicitly reported and discussed (Tiede *et al.*, 1996). The reported distributions are, however, not very different in terms of free energy. This means, that very subtle changes of conditions may have a strong influence on the observed distribution for both, experiment and calculation. We conclude, that the free energy difference between electron-transfer active and inactive conformations is close to zero and its exact value depends on the experimental conditions.

Computational results. As mentioned above, we computed the reaction energy of the electron transfer from Q_A^- to Q_B to be uphill by 157 meV in the dark-adapted x-ray structure of the bRC from *Rb. sphaeroides*. We can therefore support the assumption that the dark-adapted x-ray structure is electron-transfer inactive. Our viewpoint is exclusively thermodynamic. There may also be kinetic reasons for the inhibition of the electron-transfer in the dark-adapted x-ray structure (Stowell *et al.*, 1997), but we did not consider kinetics in the present study. In the following, we assume that the amount of electron transfer between Q_A and Q_B in the dark-adapted x-ray structure is negligibly small.

From the results above, we concluded that the equilibrium between electron-transfer active and inactive conformations prefers strongly the active conformation in the state $P^+Q_AQ_B^-$ and only weakly the inactive conformation in the ground state PQ_AQ_B (Figure 3.7). The value of the conformational equilibrium constant in the state $P^+Q_A^-Q_B$ is unknown, but it would have implications for the detailed mechanism of the conformational gating. Depending on the value of the conformational equilibrium constant, the gating mechanism may work between the following two limiting cases:

1. The equilibrium constant could be the same in the states PQ_AQ_B and $P^+Q_A^-Q_B$. Electron transfer from Q_A^- to Q_B will only occur in the small fraction of bRCs in the electron-transfer active conformation. After electron transfer, the equilibrium between electron-transfer active and inactive conformations readjusts by a conformational transition and further electron transfer

occurs with the effective rate of the conformational transition. In this mechanism, the Q_B reduction "pulls" the bRC into the electron-transfer active conformation. Hence, we call this mechanism a *pull-transition.*

2. The equilibrium constant could be the same in the states $P^+Q_A^{\cdot-}Q_B$ and $P^+Q_AQ_B^{\cdot-}$, *i. e.* already the reduction of Q_A (or other light-induced events going along with the Q_A reduction) triggers the transition to the electron-transfer active conformation (Graige *et al.*, 1998). In this case, the conformational transition from the inactive to the active conformation would also occur without the electron transfer from $Q_A^{\cdot-}$ to Q_B. The bRC is "pushed" into the electron-transfer active conformation, whether the electron transfer from $Q_A^{\cdot-}$ to Q_B will actually occur or not. We call this mechanism a *push-transition.* Since the electron-transfer reaction that leads from the state $P^*Q_AQ_B$ to the state $P^+Q_A^{\cdot-}Q_B$ is in the sub-millisecond time regime, the much slower conformational transition is still the rate-limiting step and the electron transfer reaction is therefore still gated. This rate limitation can only be circumvented by fixing the bRC in the state $P^+Q_A^{\cdot-}Q_B$, waiting until the conformational transition to the electron-transfer active conformation has occurred, and then releasing the fixation, so that the electron-transfer can proceed ungated. This procedure is, however, only a *Gedankenexperiment* and can probably not be done in reality.

The equilibrium constant between the electron-transfer active and inactive conformations in the state $P^+Q_A^{\cdot-}Q_B$ can be calculated from the difference between the calculated and experimentally measured reaction energies of the electron transfer from $Q_A^{\cdot-}$ to Q_B as shown in the following: We neglect, as mentioned above, the electron transfer between Q_A and Q_B in the electron-transfer inactive conformation. We also neglect the occupancy of the state $P^+Q_AQ_B^{\cdot-}$ in the electron-transfer inactive conformation compared to the occupancy of the same state in the electron-transfer active conformation. With these assumptions, two equilibria remain: One is the equilibrium between $P^+Q_A^{\cdot-}Q_B$ and $P^+Q_AQ_B^{\cdot-}$ in the electron-transfer active conformation with the corresponding equilibrium constant K_{AB}, and the other is the equilibrium between the electron-transfer active (*act*) and inactive (*inact*) conformations of the state $P^+Q_A^{\cdot-}Q_B$ with the corresponding equilibrium constant K_{conf} (Figure 3.7):

$$K_{AB} = \frac{[P^+Q_AQ_{B\ act}^{\cdot-}]}{[P^+Q_A^{\cdot-}Q_{B_{act}}]} = \exp\left(-\frac{\Delta G_{AB}}{kT}\right) \tag{3.12}$$

$$K_{conf} = \frac{[P^+Q_A^{\cdot-}Q_{B_{act}}]}{[P^+Q_A^{\cdot-}Q_{B_{inact}}]} = \exp\left(-\frac{\Delta G_{conf}}{kT}\right) \tag{3.13}$$

Both equilibria are reached fast compared to the recombination rate from $P^+Q_A^{\cdot-}Q_B$ to the ground state (Tandori *et al.*, 1999). In our calculation, we evaluated the equilibrium constant K_{AB}, whereas the above described experimental method to measure the equilibrium of the states $P^+Q_A^{\cdot-}Q_B$ and $P^+Q_AQ_B^{\cdot-}$ yields an equilibrium constant K_{exp} that describes the equilibrium of the states $P^+Q_A^{\cdot-}Q_B$ and $P^+Q_AQ_B^{\cdot-}$ in both conformations, the electron-transfer active and inactive. Since the occupancy of the state $P^+Q_AQ_B^{\cdot-}$ in the electron-transfer inactive conformation is neglected here, the expression of the experimentally determined equilibrium constant simplifies to

$$K_{exp} = \frac{[P^+Q_AQ_{B\ act}^{\cdot-}]}{[P^+Q_A^{\cdot-}Q_{B_{act}}] + [P^+Q_A^{\cdot-}Q_{B_{inact}}]} = \exp\left(-\frac{\Delta G_{exp}}{kT}\right) \tag{3.14}$$

The connection between the three equilibrium constants is the following:

$$K_{conf} = \frac{K_{exp}}{K_{AB} - K_{exp}} \tag{3.15}$$

Using eq 3.10, the equilibrium constants in eq 3.15 can be converted into free energy, yielding the following expression for the free energy of the conformational transition in the state $P^+Q_A^-Q_B$:

$$\Delta G_{conf} = kT \ln \left[\exp \left(\frac{\Delta G_{exp} - \Delta G_{AB}}{kT} \right) - 1 \right] \tag{3.16}$$

ΔG_{exp} is the experimentally determined reaction energy of the electron transfer from Q_A^- to Q_B derived from K_{exp}, and ΔG_{AB} is the calculated reaction energy of the electron transfer from Q_A^- to Q_B for the fixed electron-transfer active conformation derived from K_{AB}.

Since the differences between ΔG_{exp} and ΔG_{AB} is within experimental and computational uncertainty, ΔG_{conf} can only be estimated roughly. The experimental values for ΔG_{exp} range from -78 meV to -52 meV (Arata & Parson, 1981; Mancino *et al.*, 1984; Kleinfeld *et al.*, 1984a; Tandori *et al.*, 1999). The uncertainty of our computational result is very difficult to estimate because the intrinsic error of our electrostatic model is unknown. However, we assume, on the basis of our and others experiences, that our electrostatic model is sufficiently accurate to be applied successfully. We would call an electrostatic calculation of reaction energy successful, if it reproduces experimental result with an error of about ± 60 meV, which is equivalent to ± 1 pK unit. We assume this value to be the uncertainty of our computational result due to the potential error of the underlying model (but not due to statistical or numerical errors in the computational procedure itself). Hence, the value for the difference $\Delta G_{exp} - \Delta G_{AB}$ is in the range from -82 meV to +64 meV. A negative value of this difference is not possible, so that the remaining range is from 0 meV to +64 meV. A value of 0 meV corresponds to an infinitely negative value for ΔG_{conf}, which means that the electron-transfer inactive conformation is unpopulated in the state $P^+Q_A^-Q_B$ (when equilibrium is reached) and the conformational gating is done by a push-transition as described above. A value of +64 meV for the difference $\Delta G_{exp} - \Delta G_{AB}$ corresponds to a value for ΔG_{conf} of +62 meV or an equilibrium distribution of about 90 % electron-transfer inactive conformation and 10 % electron-transfer active conformation in the state $P^+Q_A^-Q_B$. Such a distribution is, at least in terms of free energy, very similar to those observed by the kinetic experiments for the ground state (Tiede *et al.*, 1996; Li *et al.*, 1998). This means, that the distribution of the electron-transfer active and inactive conformations is similar in the ground state PQ_AQ_B and in the state $P^+Q_A^-Q_B$, so that the conformational gating is done by a pull-transition.

We conclude that the free energy of the transition between electron-transfer active and inactive conformations in the state $P^+Q_A^-Q_B$ is smaller than 62 meV. Following the thermodynamic cycle in the right part of Figure 3.7, we can calculate the free energy of the transition between electron-transfer active and inactive conformations in the state $P^+Q_AQ_B^-$ to be smaller than -151 meV, which is in agreement with previous conclusions. However from our results, we cannot decide whether the conformational gating is mediated preferentially via a push-transition or a pull-transition.

Comparison to earlier computations. In the already discussed study of Alexov and Gunner (1999) the dark-adapted and light-exposed x-ray structures were not considered separately, but in one calculation where the different sidechain, Q_B, and water conformers were sampled together with the titration states by a generalized MC method. They included the two binding modes of the Q_B, distal and proximal, in the sampling. For the state $P^+Q_AQ_B^-$, Q_B was completely localized at the proximal binding site and the distal binding side was not populated in agreement with the light-exposed x-ray structure (Stowell *et al.*, 1997). For the ground state PQ_AQ_B and the state $P^+Q_A^-Q_B$, the distal binding site was occupied to 20 % and the proximal binding site to 80 %. This is in contradiction with the dark-adapted x-ray structure, which suggests that in the ground state the preferred binding site of Q_B is the distal site (Stowell *et al.*, 1997). However, as discussed above, the conformational transition from the electron-transfer inactive to the active conformation, which means mostly the movement of Q_B from the distal to the proximal binding site, is energetically very easy and may even be triggered by subtle changes in the experimental conditions. The movement of Q_B was recently observed in a

molecular dynamics simulation (Grafton & Wheeler, 1999), where it was triggered by a change of the protonation pattern of the residues Glu-L212 and Asp-L213 (see next section). So the contradiction of the computational results of Alexov and Gunner (1999) and the x-ray structure does not necessarily mean that there is a severe problem with the computational model. In agreement with our results, the electron transfer to Q_B bound at the distal site was reported to be unfavorable, but a value of the reaction energy was not provided. Alexov and Gunner (1999) proposed that possibly several smaller conformational changes and not the transition of Q_B from the distal to the proximal binding site is most important for the conformational gating process. They concluded this from their finding that the electron transfer from $Q_A^{\cdot -}$ to Q_B is uphill if they do not include conformational relaxation in their calculation (see above). However, in our studies without conformational flexibility for *Rb. sphaeroides* (Rabenstein *et al.*, 2000) and *Rps. viridis* (Rabenstein *et al.*, 1998b), we obtained energy values for the electron transfer from $Q_A^{\cdot -}$ to Q_B that are in good agreement with experimental values. The introduction of conformational relaxation (see section 3.2) for the bRC from *Rps. viridis* did not change our results fundamentally (Rabenstein *et al.*, 1998a). Hence, we disagree with the assumption that numerous but small conformational changes not represented by the different x-ray structures are necessary for the electron transfer and responsible for the conformational gating mechanism.

3.2 Conformational relaxation

3.2.1 To be investigated: again the bRC from *Rps. viridis*

It is obvious that the protein matrix of the bRC will undergo a conformational change upon electron transfer. These changes could be as dramatical as assumed for the bRC from *Rb. sphaeroides* based on the x-ray structures (Stowell *et al.*, 1997) and studied in section 3.1. However, in general the reaction after the event of an electron transfer or protonation of a titratable group are numerous small relaxation movements of molecular groups in the neighborhood of the transition. Alexov and Gunner (1999) even propose such relaxation movements as the conformational gating step for the electron transfer from $Q_A^{\cdot -}$ to Q_B in the bRC. In calculations with a single, rigid structure, these relaxations can be represented by an increased dielectric constant ε_p for the protein interior.

In this section, I will present a method we developed for simulating the relaxation explicitly by an energy minimization scheme. We applied this method to study as before the bRC from *Rps. viridis* at pH 7.5 with its quinones in the states Q_AQ_B, $Q_A^{\cdot -}Q_B$, $Q_AQ_B^{\cdot -}$, $Q_A^{\cdot -}Q_B^{\cdot -}$, and $Q_AQ_B^{2-}$. We will show that after the explicit relaxation, the dielectric constant can indeed be reduced from $\varepsilon_p = 4$ to $\varepsilon_p = 2$.

In one previous study at the bRC of *Rps. viridis*, an energy minimization scheme was already used to obtain relaxed protein conformations (Cometta-Morini *et al.*, 1993). In that work, also the bRC state, where the Q_B is singly reduced and singly protonated ($Q_B^{\cdot}H$), was considered. However, only a small part of the bRC near Q_B was included in that computation, and the minimization was performed with the titratable amino acids in their standard protonation state (at pH 7 in solution). Also no reaction energies for electron transfer were calculated.

3.2.2 Methods

3.2.2.1 Structural relaxation

In the conventional method for calculating protonation patterns, structural relaxation upon changes in the electrostatic potential is not considered explicitly. Instead, it is incorporated only in an average way by using a dielectric constant of $\varepsilon_p \geq 4$, which accounts for electronic as well as for nuclear polarization effects (Warshel & Russel, 1984; Warshel *et al.*, 1997). The latter are due to reorientation of charged and polar molecular groups. If only electronic polarizability is taken into account, the

dielectric constant is assumed to be ε_p=2, based on the high-frequency dielectric constant of apolar organic liquids (Sharp & Honig, 1990).

In our method, nuclear polarization effects are treated explicitly by structural relaxation. This is achieved in the following manner:

1. To get reasonable starting values for the protonation pattern at a given pH value, a conventional calculation with ε_p=4 is performed, using the original unrelaxed crystal or NMR structure.

2. Now the atomic partial charges of the titratable groups are assigned according to their fractional protonation. These atomic partial charges are obtained by a linearly weighted average of the charges of the protonated and deprotonated state. Starting with this charge assignment, we energetically minimized the structure using the program CHARMM (Brooks *et al.*, 1983). To save CPU-time, we used homogeneous dielectrics for the energy minimization, which are valid only approximately. To avoid artifacts due to energy minimization, protein atoms close to the surface are spatially constrained.

3. Next, the calculation of the protonation pattern is repeated with the minimized structure. However, the dielectric constant for the protein is now set to a value of ε_p=2, since the nuclear polarization is taken into account by the structural relaxation, which occurs during the minimization procedure.

4. Steps 2 and 3 are repeated iteratively, until the calculated fractional protonation of each individual titratable group differs less than a tenth of a proton between subsequent iteration steps providing selfconsistency of structure and protonation pattern. Figure 3.8 summarizes the algorithm.

Note that the energy minimization in step 2 is performed with the protonation pattern calculated in the previous step, but with the original structure as starting conformation. In the absence of thermal fluctuations, protonation patterns and conformations are able to stabilize each other, so that rather artificial conformations become possible. Therefore, for each minimization the original unrelaxed structure is used as starting conformation in order to prevent that during the iteration procedure the structure drifts into conformations that are too far away from the original structure.

For the energy minimizations, the Coulomb and Lennard-Jones interactions were calculated with a cut-off radius of 10.0 Å using group shift cut-off conditions. All atoms with a distance of more than 20 Å from the non-heme iron were constrained to their position of the original structure by a harmonic potential with a force constant of 0.42 kJ mol^{-1} Å^{-2}. We did not add water molecules to the system, but in contrast to the electrostatic calculations, the water molecules contained in the crystal structure were included in the energy minimization. These water molecules fill cavities in the protein and can thus account for an otherwise heterogeneous dielectric medium (Ullmann *et al.*, 1996), which cannot be handled with CHARMM. For each minimization procedure, we performed 1000 steps of energy minimization with steepest descent, followed by 2000 steps with the conjugated gradient method.

3.2.2.2 Calculating the energy of electron transfer for the relaxed conformations

At first, we calculated the protonation patterns as before and applied the relaxation procedure to the bRC with a fixed quinone state (Q_AQ_B, $Q_A^{\cdot-}Q_B$, $Q_AQ_B^{\cdot-}$, $Q_A^{\cdot-}Q_B^{\cdot-}$, or $Q_AQ_B^{2-}$). This yielded a different conformation for each bRC state. Thus, in order to calculate the energy of the electron transfer from Q_A to Q_B, we had to consider two different conformations together. We did this by using the method described in section 3.3. This requires to determine the value of ΔG^l_{conf} (see eq 3.19 on page 69) for each bRC state. This value represents the relative conformational energy of the protonation reference state of conformation l, *i.e.* of the state, where all titratable groups are in their uncharged

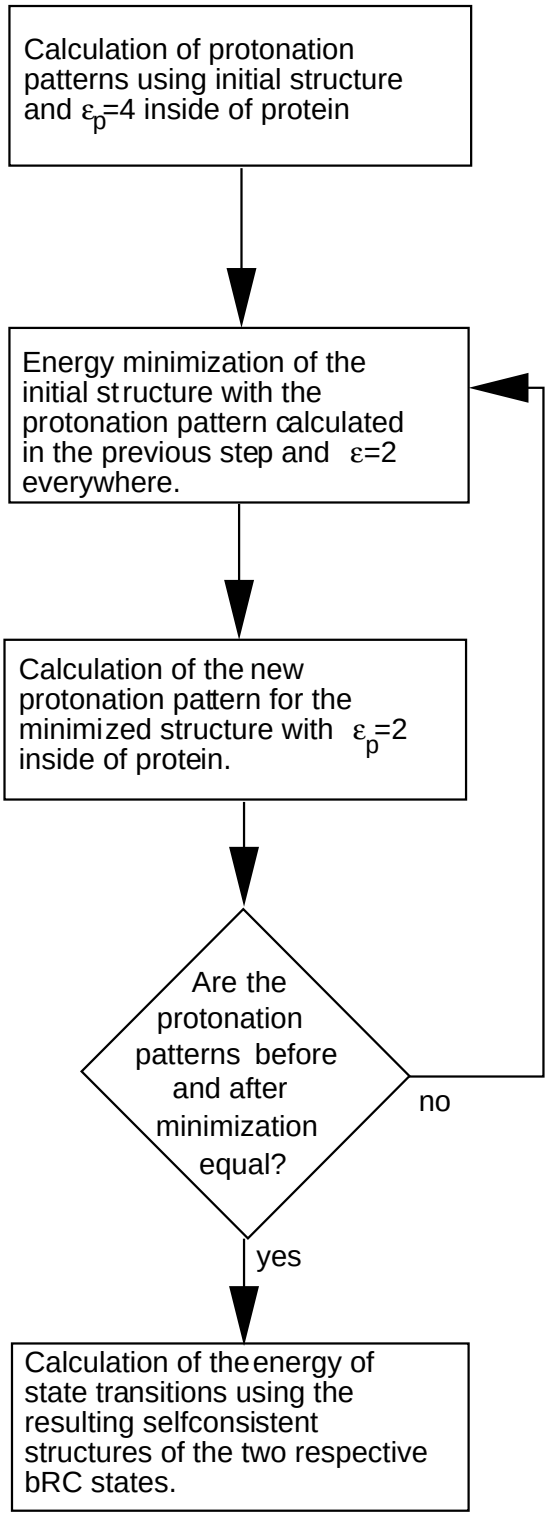

Figure 3.8: Overview of the complete relaxation procedure.

protonation state. The energy of one conformation can be chosen arbitrarily. Hence, ΔG^{l}_{conf} can be considered as the energy difference between the conformational energy of the conformation l itself and the energy of an arbitrarily chosen reference structure. This energy difference can be obtained

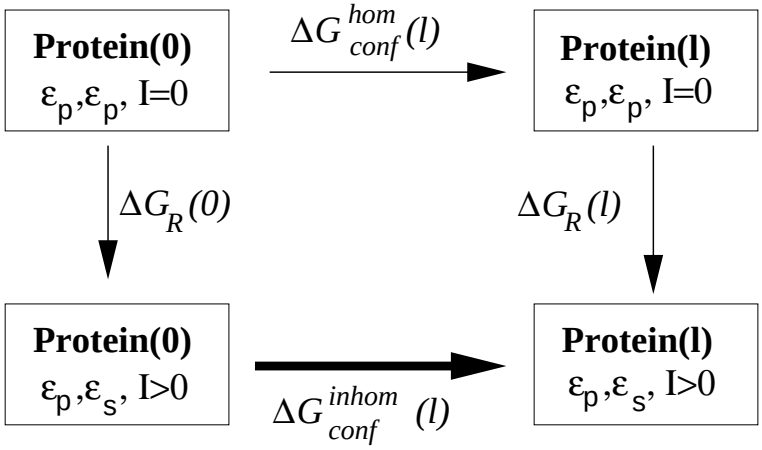

Figure 3.9: Thermodynamic cycle to calculate the conformational energy.

via the thermodynamic cycle depicted in Figure 3.9 resulting in eq 3.17 (where $G^{inhom}_{conf}(l)$ is identical to ΔG^{l}_{conf}, the superscript *inhom* emphasizes that this energy is calculated for an inhomogeneous dielectric medium).

$$\Delta G^{inhom}_{conf}(l) = G^{inhom}_{conf}(l) - G^{inhom}_{conf}(0) = \Delta G^{hom}_{conf}(l) + \Delta G_R(l) - \Delta G_R(0) \tag{3.17}$$

According to Figure 3.9, the protein with a dielectric constant ε_p is brought from a medium with homogeneous dielectrics, where the ionic strength is $I = 0.0$ and the dielectric constant is ε_p everywhere, into the solvent with a dielectric constant ε_s and a ionic strength $I \geq 0$. In the homogeneous medium, we obtained the conformational energy difference $\Delta G^{hom}_{conf}(n)$ simply from the CHARMM force field (Brooks *et al.*, 1983). To distinguish the conformational energy in a homogeneous medium from the needed conformational energy in a inhomogeneous medium, these to energies are labeled as $\Delta G^{hom}_{conf}(n)$ and $\Delta G^{inhom}_{conf}(n)$, respectively. The energy ΔG_R (eq 3.18) is required to bring a molecule from a medium with a dielectric constant of ε_p and ionic strength $I = 0.0$ into a medium with a dielectric constant of ε_s and ionic strength $I \geq 0$.

$$\Delta G_R = \frac{1}{2}\sum_{i=1}^{N} q_i[\phi(\vec{r}_i, \varepsilon_p, \varepsilon_s, I) - \phi(\vec{r}_i, \varepsilon_p, \varepsilon_p, 0.0)] \tag{3.18}$$

In eq 3.18, $\phi(\vec{r}_i, \varepsilon_p, \varepsilon_s, I)$ is the solution of the PBE (section 1.1) with dielectric constants ε_p for the protein and ε_s for the solvent and ionic strength I at the place of charge q_i using the charge distribution of the reference protonation-state. The sum in eq 3.18 runs over all charges of the molecular system in the reference protonation-state. The program MEAD, which we used to calculate intrinsic pK_a values, is also capable to calculate this energy. However, since the electrostatic potential of the whole molecule is needed, the grid used for solving the PBE must now be large enough to contain the whole bRC even at the finest focusing level. We used initially a 200 Å cube grid with a 2.0 Å lattice spacing, followed by a 100 Å cube grid with a 0.5 Å lattice spacing. The centers of both grids were placed on the geometrical center of the bRC.

A thermodynamic cycle similar to the one depicted in Figure 3.9 has previously been used to calculate relative binding constants of diprotein complexes (Ullmann *et al.*, 1997).

3.2.3 Results and Discussion

3.2.3.1 Improved MC sampling with triple moves

As already mentioned in section 3.1.2.4, the stronger coupling due to the low dielectric constant of $\varepsilon_p = 2$ leads to sampling problems, which can be solved by introducing triple moves. In Table 3.8, examples for residues with sampling problems are shown, when the calculations were performed with single moves only, with single and double moves, and with single, double and triple moves. For some residues, the sampling problems with single moves or single and double moves were so strong, that no statistical uncertainty could be calculated. For the calculation of the statistical uncertainty as described in section 3.1.2.4, the correlation time is needed (eq 3.8 and 3.9). The correlation time, however, cannot be calculated, if the correlation function does not reach a lower limit. As can be seen in Table 3.8, the introduction of double moves fixes some, but not all of the sampling problems. After introduction of triple moves, sampling problems did not occur any longer, and the statistical uncertainty was less than 0.01 for all residues.

Table 3.8: Examples of residues with MC sampling problems. Given are the protonation probabilities with statistical uncertainty ($\pm 1\sigma$) for three residues with sampling problems in the first iteration of the $Q_A^- Q_B$ state, calculated from MC sampling with single, double and triple moves.

residue	single	double	triple
Glu-M171	$(0.690)^a$	$(0.726)^a$	0.649 ± 0.005
δ-His-H9	$(0.660)^a$	0.742 ± 0.005	0.741 ± 0.005
δ-His-M162	$(0.314)^a$	$(0.278)^a$	0.354 ± 0.005

[a] Result is not converged, statistical uncertainty could not be calculated.

3.2.3.2 Relaxed selfconsistent structures

Consistency of energy minimized structure and protonation pattern was reached after eight iterations for each bRC state. We calculated root mean square deviations (rmsd) of the final structures corresponding to different bRC states relative to the original structure and relative to each other (Table 3.9). To align two structures, we used the algorithm of Kabsch (1976). Water molecules were not considered in the calculation of rmsd.

Table 3.9: Root mean square deviations (rmsd, in Å) of the relaxed structures respective to the crystal structure (column "x-ray") and to each other. Water molecules are not included in the calculation of the rms deviation.

structure	x-ray	$Q_A Q_B$	$Q_A^- Q_B$	$Q_A Q_B^-$	$Q_A^- Q_B^-$	$Q_A Q_B^{2-}$
$Q_A Q_B$	0.670	0.000	0.096	0.096	0.154	0.122
$Q_A^- Q_B$	0.668	0.096	0.000	0.132	0.174	0.147
$Q_A Q_B^-$	0.665	0.096	0.132	0.000	0.132	0.109
$Q_A^- Q_B^-$	0.671	0.154	0.174	0.132	0.000	0.130
$Q_A Q_B^{2-}$	0.676	0.122	0.147	0.109	0.130	0.000

The rmsd of the final selfconsistent structures relative to the crystal structure, averaged over all atoms, is about 0.67 Å for all bRC states. However, the minimized structures are not equal for the

different bRC states. The rms deviation among the minimized structures is up to 0.17 Å. Although Stowell *et al.* (1997) recently reported dramatic conformational changes upon the first electron transfer from Q_A to Q_B (see also section 3.1), the conformational changes calculated here are relatively small. This is not surprising, since minimization is only able to find the next minimum, but not to overcome energy barriers, which is necessary to obtain larger conformational changes. To consider larger conformational changes, molecular dynamics or MC dynamics may be useful (see chapter 4).

3.2.3.3 Total protonation and individual site protonation

Table 3.10 shows the protonation probability of all non-standard protonated residues that are less than 25 Å away from the quinones. Furthermore, the difference in total protonation between the ground state Q_AQ_B of the bRC and the respective other states are listed. Significant differences in the protonation pattern near the quinones between the original structure before relaxation (with ε_p=4) and the final selfconsistent structures after relaxation (with ε_p=2) occurred only at four residues (Glu-H177, Glu-H234, His-L211, His-M16). The histidines changed between δ and ε tautomer, but they remained nearly unprotonated. The two glutamates changed from an intermediate protonation

Table 3.10: Total protonation of the bRC and individual site protonations at pH 7.5 before relaxation by energy minimization (ε_p=4) and after relaxation (ε_p=2). All residues within a distance of 25 Å from one of the two quinones and with at least 0.05 protons deviation from standard protonation are shown, except N-termini of L- and M-chain which are completely deprotonated in all states before and after relaxation. For histidines, not the protonation, but the fraction of δ-/ε-tautomer is given. The remaining part (one minus fraction of δ tautomer minus fraction of ε tautomer) is the fraction of protonated histidine (*i.e.* with a proton at the δ-N and at the ε-N). Histidines protonated only at $N_{\varepsilon 2}$ are considered to be in standard protonation and not included in the table.

residue	relaxation	Q_AQ_B	$Q_A^{\cdot-}Q_B$	$Q_AQ_B^{\cdot-}$	$Q_A^{\cdot-}Q_B^{\cdot-}$	$Q_AQ_B^{2-}$
Glu-H45	before	0.05	0.06	0.05	0.06	0.05
	after	0.00	0.00	0.00	0.00	0.00
Glu-H97	before	0.01	0.01	0.01	0.01	0.01
	after	0.03	0.04	0.06	0.04	0.03
Glu-H177	before	0.03	0.06	0.59	0.80	0.99
	after	1.00	1.00	1.00	1.00	1.00
Glu-H234	before	0.27	0.30	0.26	0.27	0.25
	after	0.98	0.98	0.98	0.99	0.98
Glu-L104	before	1.00	1.00	1.00	1.00	1.00
	after	1.00	1.00	1.00	1.00	1.00
Glu-L212	before	0.99	0.99	1.00	1.00	1.00
	after	1.00	1.00	1.00	1.00	1.00
His-L211	before	0.47/0.53	0.50/0.50	0.53/0.47	0.53/0.47	0.58/0.42
	after	0.86/0.14	0.91/0.09	0.95/0.05	0.95/0.05	0.98/0.02
His-M16	before	0.25/0.73	0.25/0.72	0.25/0.73	0.25/0.73	0.24/0.74
	after	0.13/0.87	0.13/0.87	0.14/0.86	0.15/0.85	0.14/0.86
all[1]	before	0.00	0.14	0.60	0.88	0.97
	after	0.00	0.02	0.05	0.02	0.03

[1]expressed as difference to the ground state Q_AQ_B, statistical uncertainty ($\pm 1\sigma$) is ± 0.02

probability in the original structure to a (nearly) complete protonation in the relaxed structure. Hence, our relaxation method tends to stabilize fully deprotonated or protonated states, as can also be seen less pronounced for most of the other residues. Glu-H177 and Glu-H234 are responsible for most of the change in total protonation for the unrelaxed structure. Due to the described stabilization effect, for the relaxed structures, both residues are almost fully protonated in all bRC states. Hence, the stabilization effect is responsible for the much smaller changes in total protonation of the bRC, if structural relaxation is applied (see last two rows of Table 3.10). At a first glance, this effect seems surprising, since a decrease of electrostatic screening by reducing the dielectric constant of the protein from ε_p=4 to ε_p=2 will lead to increased differences in the protonation pattern due to changing the redox state of the quinones. The structural relaxation seems to replace the dielectric screening by using the larger dielectric constant of ε_p=4. As a further consequence, changes in total protonation were reduced to values as small as the statistical uncertainty. However, the absence of proton uptake upon changing of the initial state Q_AQ_B is not in agreement with experimental results. At pH 7.5, Maróti and Wraight (1988) and McPherson *et al.* (1988) measured both an total proton uptake of 0.34 for the transition from the Q_AQ_B-state to the $Q_A^{\cdot-}Q_B$-state of the bRC of *Rb. sphaeroides*. Sebban *et al.* (1995) measured this value at the bRC of *Rb. capsulatus* to be 0.24 protons. Using an unrelaxed bRC structure, the calculated value of the total proton uptake agrees better with experimental results. The proton uptake for the transition from the Q_AQ_B-state to the $Q_AQ_B^{\cdot-}$-state was determined to be 0.37 by McPherson *et al.* (1988) and 0.90 by Maróti and Wraight (1988). Both values were measured with the bRC of *Rb. sphaeroides*. The proton uptake upon the first electron transfer from Q_A to Q_B ($Q_A^{\cdot-}Q_B \rightarrow Q_AQ_B^{\cdot-}$) is therefore 0.03 (McPherson *et al.*, 1988) or 0.56 (Maróti & Wraight, 1988). From our calculations, we got a value of 0.46 protons with the unrelaxed structure and 0.03 with the relaxed structures. Hence, in this case the results from the relaxed structures agree with the measurements of McPherson *et al.* (1988), while the results from the unrelaxed structure agree with the measurements of Maróti and Wraight (1988). In addition to the problem that different experimental groups obtained different results, a comparison with these experimental data may be problematic due to the differences between the bRC of *Rps. viridis* used in our calculations and the bRC's of the purple bacteria used in the experiments (*Rb. sphaeroides* or *Rb. capsulatus*). Also a partial protonation of the charged quinones may contribute to the experimental values, but was not considered in our study.

3.2.3.4 Energetics of the electron transfers

We considered here the first and the second electron transfer from Q_A to the unprotonated Q_B. The first electron transfer is the transition from the $Q_A^{\cdot-}Q_B$-state to the $Q_AQ_B^{\cdot-}$-state. We calculated the driving force of the electron transfer with these two structures using the method described in section 3.3 (see below). The reference protonation and redox state of both structures, used in the electrostatic calculation and in the calculation of the relative conformational energy, is the state where all titratable groups are in their uncharged protonation state and the quinones are in the redox state $Q_AQ_B^{\cdot-}$. The conformation obtained by minimizing the energy with the quinones in the $Q_AQ_B^{\cdot-}$-state is considered as conformation 0 according to Figure 3.9. Then we obtained -16 kJ/mol for $\Delta G_{conf}^{hom}(l)$. $\Delta G_R(0)$ is 20 kJ/mol lower than $\Delta G_R(n)$, so that $G_{conf}^{inhom}(l)$ is +4 kJ/mol. We used this value to calculate the reaction energy of the first electron transfer, yielding -95 mV (9.2 kJ/mol). If no structural relaxation was applied, *i. e.* using only the original structure with ε_p=4, we calculated an energy value of -160 meV (section 3.1.3.2). Experimentally a value of about -150 meV was measured for the bRC of *Rps. viridis* (Baciou *et al.*, 1991). The value from the calculation without structural relaxation is not necessarily better than the value obtained from the calculation with relaxation, since the deviation of both values from the experimental value are within experimental uncertainty. Baciou *et al.* (1991) measured also that the energy of the first electron transfer is approximately the same at pH 7.5 and pH 9. At pH 9, another group determined this energy to be about -120 meV (Shopes & Wraight,

1985), which is closer to the value calculated with structural relaxation. In analogy to the results for the protonation pattern, the calculation of the reaction energy of the first electron transfer yields similar results with the relaxation procedure and a dielectric constant of ε_p=2 for the protein as without relaxation and ε_p=4.

For the second electron transfer, the bRC structures of the states $Q_A^{\cdot-}Q_B^{\cdot-}$ and $Q_AQ_B^{2-}$ were considered. The reference protonation and redox state of both structures is the state where all titratable groups are in their uncharged protonation state and the quinones are in the redox state $Q_AQ_B^{2-}$. The conformation obtained by minimizing the energy with the quinones in the $Q_AQ_B^{2-}$-state is considered as conformation 0 according to Figure 3.9. We obtained +206 kJ/mol for $\Delta G_{conf}^{hom}(l)$. $\Delta G_R(0)$ is 13 kJ/mol higher than $\Delta G_R(n)$, so that $G_{conf}^{inhom}(l)$ is +193 kJ/mol. Together with the electrostatic calculation, this resulted in a total reaction energy of +1,2 eV (120 kJ/mol) for the second electron transfer from Q_A to the unprotonated Q_B. Without relaxation (section 3.1.3.3), we calculated an energy value of +1,1 eV (110 kJ/mol). Again, without structural relaxation and ε_p=4, the results are similar to the results with structural relaxation and ε_p=2. The result also supports our conclusion from section 3.1, where we found that the reaction energy for the second electron transfer from Q_A to the unprotonated Q_B is too large to allow a doubly reduced, unprotonated Q_B as a thermally accessible intermediate. Hence, the second electron transfer will not occur before protonation of the singly reduced Q_B. Even with explicit consideration of structural relaxation, our conclusions obtained from unrelaxed bRC structures remain unchanged.

3.2.3.5 The dielectric constant within the protein

The value of the dielectric constant ε_p taken for the protein varies considerably, ranging from ε_p=1 (Muegge *et al.*, 1996; Scarsi *et al.*, 1997) to ε_p=20 and larger (Warshel *et al.*, 1984; Antosiewicz *et al.*, 1994; Demchuk & Wade, 1996). A high dielectric constant seems to yield better agreement with experimental data, if simplified descriptions of the protein charges are used (Antosiewicz *et al.*, 1994). In those calculations, the protonation of a titratable amino acid is modeled by simply placing a unit charge at a central atom of the titratable site. With a more detailed charge model, where several atomic partial charges of the titratable residue are changed upon protonation, good agreement with experimental data was achieved by using a dielectric constant of ε_p=4 (Bashford *et al.*, 1993; Antosiewicz *et al.*, 1996). Apparently, the large value of the dielectric constant ($\varepsilon_p \geq 20$) was necessary to compensate the effects from an unrealistic charge distribution, where a unit charge is placed at a central atom of the titratable site. The dielectric constant of ε_p=4 can be rationalized as follows: A factor of 2 accounts for the effects of electronic polarization, another factor of 2 or more for the effects of nuclear polarization, *i. e.* for the reorientation of dipoles and displacements of atoms (Warshel & Russel, 1984; Warshel & Åqvist, 1991; Honig & Nicholls, 1995; Warshel *et al.*, 1997). The method presented here considers reorientation and relaxation effects explicitly. The application demonstrates that the results from a conventional calculation with a detailed charge model and a dielectric constant of ε_p=4 without structural relaxation are similar to the results from a calculation with a dielectric constant of ε_p=2 with structural relaxation. Thus, our results support the rationalization given above.

Another interesting study to understand the value of ε_p was done by Demchuk and Wade (1996). They analyzed the dependence of calculated pK_a values on the dielectric constant carefully and made the interesting observation that a large dielectric constant led to better agreements with experiments for residues that are on the surface of the proteins, while for residues that are buried in the protein better results were obtained with a small dielectric constant. This observation is in good agreement with calculation of the dielectric constants in proteins (Simonson *et al.*, 1992; Simonson & Perahia, 1995a, 1995b; Simonson & Brooks, 1996). The dielectric constant at the more flexible surface of proteins turned out to be about 10 to 20, while it was about 2 to 4 in the interior of the protein. Consideration of individual water molecules in computations of pK_a values in proteins do not improve

the agreement with experimental results (Gibas & Subramaniam, 1996). This result may be due to the unknown orientation of water molecules in crystal structures (Ullmann *et al.*, 1996; Rabenstein *et al.*, 1998b, 1998a; Kannt *et al.*, 1998). Furthermore, water molecules may reorient when a nearby titratable group changes its protonation. A promising method to include this in titration calculations was applied by Alexov and Gunner (1999).

3.2.4 Concluding remarks

We have to keep in mind that with the present procedure to calculate protonation patterns the initial protonation pattern obtained with the higher dielectric constant $\varepsilon_p = 4$ and the unrelaxed structure tends to be stabilized, even if this protonation pattern is wrong. A related effect could be observed by Wlodek *et al.* (1997).

Individual titratable groups that are partially protonated in the unrelaxed protein structure tend to be fully protonated or deprotonated in the selfconsistently relaxed structure, leading to a structure and protonation pattern of lower energy. This may be a result of the structural relaxation method, where the protonation pattern and the structure are energetically minimized, corresponding effectively to a dynamic at vanishing temperature and therefore correlating structure and protonation pattern too strongly. With an molecular ensemble at non-vanishing temperature, these correlations are reduced due to suitable entropic contributions. Such an ensemble cannot be generated easily with molecular dynamics solving Newton's equation of motion. During an MD simulation, it is impossible to change the protonation pattern discontinuously. This problem does not occur with MC dynamics as presented in chapter 2. A combination of titration and MC dynamics is outlined in chapter 4.

MC dynamics will also solve another problem which appears with structural relaxation by energy minimization. In contrast to energy minimization, MD and MC dynamics are able to overcome energy barriers. This is often necessary, even if only apparently small conformational changes are involved. To demonstrate this, we tried to calculate also the energetics of protonation reactions of the Q_B in the bRC (results not shown). Our relaxation procedure was not able to give energetically favorable selfconsistent structures for the protonated states of Q_B, so that the states where Q_B was unprotonated were favored strongly against those states where Q_B was protonated, resulting in an unrealistic high energy for the protonation of Q_B. A similar result was obtained by Cometta-Morini *et al.* (1993), who also applied a minimization scheme for structural relaxation and found that the singly reduced Q_B is completely deprotonated over the pH range from 6 to 11. Assuming that for the protonation of Q_B a conformational energy barrier must be overcome, energy minimization is not sufficient to obtain properly relaxed structures. Therefore, a relaxation procedure needs to be applied that generates protein conformations at non-vanishing temperatures.

3.3 Titration of an ensemble of protein conformations

3.3.1 To be investigated: carbonmonoxymyoglobin

Myoglobin is one of the most widely studied proteins. Numerous x-ray structures with different myoglobin ligands and under different physical conditions were solved in the past. In this section, we focus on a set of structures of sperm whale carbonmonoxymyoglobin (MbCO) that are prepared at pH values of 4, 5, and 6 (Yang & Phillips Jr., 1996). This set of structures shows that at low pH, His-64 – an important residue for O_2 specificity (Springer *et al.*, 1994) – swings out of the CO binding pocket. It is assumed that a protonation of His-64 goes along with this remarkable conformational change (Yang & Phillips Jr., 1996; Johnson *et al.*, 1996).

The protonation behavior of myoglobin has been studied extensively by theoretical methods (Shire *et al.*, 1975; Bashford *et al.*, 1993; Yang & Honig, 1994; Sandberg & Edholm, 1999). How-

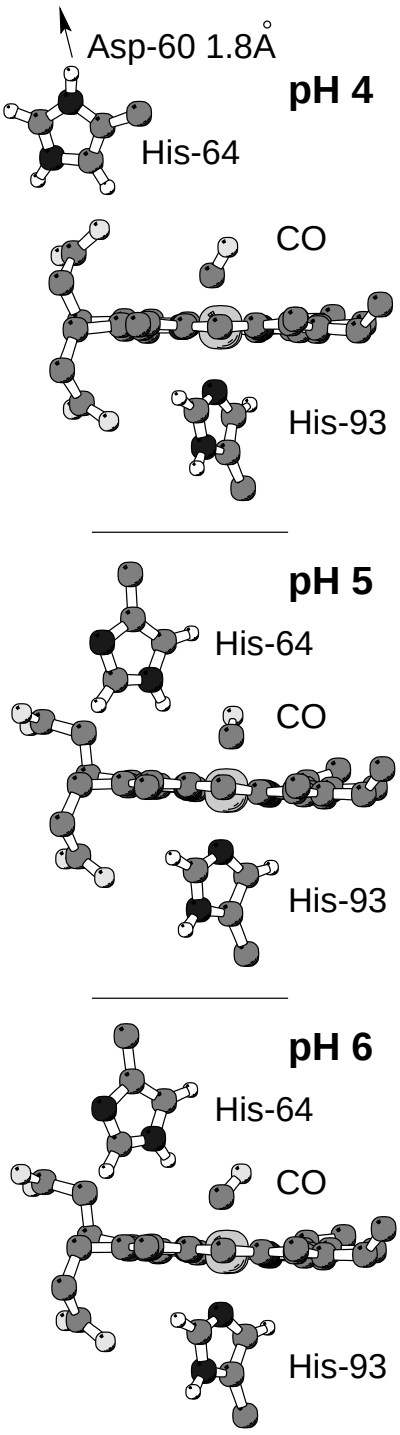

Figure 3.10: Heme, CO ligand, and sidechains of His-64 and His-93 from the three MbCO x-ray structures at pH 4, 5, and 6. Hydrogen atoms of the heme are not drawn for the sake of clarity. The main feature of the structural changes is the rotation of His-64 out of the CO binding pocket at low pH. According to our results, protonation of His-64 goes along with this rotation. The unprotonated His-64 prefers the ε tautomeric form.

ever, in these studies conformational flexibility was not considered explicitly.

3.3.2 Methods

To take into account the structural differences within the set of x-ray structures, the continuum electrostatics method must be extended to include an ensemble of multiple conformations (Ullmann & Knapp, 1999). There are numerous approaches to include multiple conformations in the calculations of protonation behavior (Buono *et al.*, 1994; You & Bashford, 1995; Beroza & Case, 1996; Sham *et al.*, 1997; Schaefer *et al.*, 1997; Alexov & Gunner, 1997, 1999). However, these methods are not feasible here, since they account only for conformational changes of titratable groups, explicitly simulated water molecules, and/or hydrogens. Here, a small number of protein structures is given with completely different sets of atomic coordinates. Hence, not only atoms of the backbone and non-titratable groups are displaced, but also the dielectric boundary is changed. In this section, we present a new method to treat a given ensemble of a small number of arbitrarily different conformers of a protein.

3.3.2.1 Coordinates and parameters

In our calculations, we used x-ray structures of sperm whale carbonmonoxymyoglobin (MbCO) at pH values 4, 5, and 6 (Yang & Phillips Jr., 1996). The PDB identifiers and resolutions of these structures are 1spe and 2.0 Å for pH 4, 1vxc and 1.7 Å for pH 5, and 1vxf and 1.7 Å for pH 6. For the residues 79 to 81, the structures 1spe and 1vxc contain two alternative conformations A and B, which we considered separately. Thus, we got five different structures called in the following 4a, 4b, 5a, 5b, and 6, with the digit corresponding to their respective pH value of preparation and the letter corresponding to the conformation of the residues 79 to 81. As before, we removed the sulfate ion and all water molecules from each structure. We considered as titratable groups the C-terminus, the N-terminus, the two propionates of the heme, and all aspartates, glutamates, arginines, lysines, tyrosines, and histidines, with the exception of His-93, which coordinates the heme iron and is therefore considered to be non-titrating. Different to the extended-atom model used before, we used for MbCO an all-atom model where all hydrogen atoms were treated explicitly with the exception of the hydrogen atom of protonated carboxyl groups. In this case, the hydrogen atom was treated implicitly by distributing its charge symmetrically to the two oxygen atoms of the carboxyl group. The coordinates of hydrogen atoms were generated with CHARMM (Brooks *et al.*, 1983). The positions of hydrogen atoms were energetically optimized using the CHARMM program with the CHARMM22 force field (MacKerell *et al.*, 1992), while the heavy atom positions were fixed. For this optimization, all titratable groups were in their standard protonation (*i.e.*, aspartate, glutamate, heme-propionate and the C-terminus unprotonated, arginine, histidine, lysine, tyrosine and the N-terminus protonated). All atomic partial charges, including that of the heme, and the atomic radii were taken from the CHARMM22 force field (MacKerell *et al.*, 1992). However, we needed to apply some modifications and endorsements: As mentioned above, the proton of protonated carboxyl groups is not represented explicitly, but simply by symmetrically distributing its charge to the atoms of the unprotonated carboxyl group (Table 3.11). We did this since we cannot know the exact binding site of the proton. A more detailed approach would be to introduce more than two states for a titratable group similar to the way it was done for histidines here (Bashford *et al.*, 1993; Beroza & Case, 1996; Alexov & Gunner, 1997). For similar reasons, the deprotonation of Arg, Lys, and the N-terminus was represented by symmetrically removing a unit positive charge from the atoms of the titratable group (Table 3.11). For the charges of deprotonated tyrosine, which are not part of the CHARMM22 parameter set, we based our charges on quantum chemical calculations as described above. Atomic partial charges that are not explicitly part of the CHARMM22 parameter set are listed in Table 3.11.

Table 3.11: Atomic partial charges of titratable groups.

Group	protonated	deprotonated
Carboxyl (except C-term.)		
C-α	-0.21	-0.28
carboxyl C	0.75	0.62
carboxyl O (2x)	-0.36	-0.76
C-terminus		
carboxyl C	0.34	0.34
carboxyl O (2x)	-0.17	-0.67
Arginine		
N-ε	-0.70	-0.81
C-ζ	0.64	0.71
guanidino N (2x)	-0.80	-0.90
guanidino H (4x)	0.46	0.27
Lysine/N-terminus		
amino N	-0.30	-0.97
amino H (3x)	0.33	0.22
Tyrosine		
C-ζ	0.11	-0.18
hydroxyl O	-0.54	-0.82
hydroxyl H	0.43	0.00

3.3.2.2 Titration of single conformers

First, we calculated the protonation pattern of all five structures separately. This was done as described before. For the solvation of the PBE, we performed this time grid focussing (Klapper *et al.*, 1986) in two steps. Initially, we used a 80 Å-cube with a 1.0 Å lattice spacing centered at the geometric center of the protein, followed by a 20 Å-cube with a 0.25 Å lattice spacing centered at the considered titratable group. All other parameters were the same as in the previous calculations.

The number of titratable residues of MbCO is only 73, not about 200 as for the bRC above. However, the number of possible protonation states is still too large to be calculated exactly. Therefore, we used again the MC sampling with the same parameters as before. However, this time we did one complete sampling for each 0.1 pH increment in the range from pH 3 to pH 7. For each sampling, we performed 10,000 full scans and after that 100,000 so-called reduced scans. The statistical error for each single group was smaller than 0.003, and the statistical error of the total protonation of the whole myoglobin was always smaller than 0.05 protons.

3.3.2.3 Titration of a conformational ensemble

To account for conformational variability in computations of electrostatic energies, Eq. 3.1 must be modified, yielding Eq. 3.19, which is the energy $G^{n,l}$ of the protonation state n in a certain conformation l (Ullmann & Knapp, 1999).

$$G^{n,l} = \sum_{\mu=1}^{N} \left((x_\mu^n - x_\mu^o) RT \ln 10 (\mathrm{pH} - \mathrm{p}K_{intr,\mu}^l) + \sum_{\nu>\mu}^{N} W_{\mu\nu}^l (x_\mu^n - x_\mu^o)(x_\nu^n - x_\nu^o) \right) + \Delta G_{conf}^l \qquad (3.19)$$

The interaction parameters $pK^l_{intr,\mu}$ and $W^l_{\mu\nu}$ depend now on the actual conformation l. The conformational reference energy $\Delta G^l_{conf} = G^l_{conf} - G^r_{conf}$ is the energy difference between an arbitrarily chosen, albeit fixed, reference conformation r and the actual conformation l. For the computation of ΔG^l_{conf}, the protein must be in its reference protonation state for both conformations r and l, *i. e.*, all titratable groups are in their uncharged protonation state. If there are L conformations in the conformational ensemble, the total number of combined protonation and conformational states is $L \cdot 2^N$ (with N being the number of titratable groups). The thermodynamic average in Eq. 3.7 must now be evaluated for all $L \cdot 2^N$ states yielding Eq. 3.20 (Rabenstein *et al.*, 1998a).

$$\langle x_\mu \rangle = \frac{\sum_{l=1}^{L} \sum_{n=1}^{2^N} x_\mu^n \exp(-G^{n,l}/RT)}{\sum_{l=1}^{L} \sum_{n=1}^{2^N} \exp(-G^{n,l}/RT)} \tag{3.20}$$

The occupation probability α_m of a certain conformation m within the conformational ensemble can also be calculated by a thermodynamic average:

$$\alpha_m = \frac{\sum_{n=1}^{2^N} \exp(-G^{n,m}/RT)}{\sum_{l=1}^{L} \sum_{n=1}^{2^N} \exp(-G^{n,l}/RT)} \tag{3.21}$$

Again, the thermodynamic average can only be calculated analytically for a small number of titratable groups and conformations as it was done by Rabenstein *et al.* (1998a). However, in the case of MbCO, the number of titratable groups is $N = 73$ and the number of conformations is $L = 5$, so that the number of states is $5 \cdot 2^{73}$. We sampled also this increased number of states by an MC method. We did this by introducing conformational MC moves in addition to the titration moves. However, in doing so, the conformational sampling proved to be not efficient enough. To overcome this problem, we applied parallel tempering (Geyer, 1991).

3.3.2.4 Parallel tempering

In parallel tempering (Geyer, 1991), the MC simulation is not performed for a single system, but for I non-interacting systems in parallel. Each system is a copy of the original single system with the only difference in temperature T. The systems are numbered from 1 to I in a way that $T_{i+1} > T_i$ (with $0 \leq i < I$). Titration and conformational moves are applied as before to each of the parallel systems independently. However, a third kind if move is introduced, a so-called tempering move (Figure 3.11). This move exchanges the protonation state $\vec{x}_i$ and the conformation l_i of a randomly selected system i ($i < I$) with the protonation state $\vec{x}_{i+1}$ and the conformation $l_{i+1}$of system $i+1$. A tempering move is accepted with the probability

$$p = \min\left[1, \exp\left(R^{-1}\left(T_i^{-1} - T_{i+1}^{-1}\right)(G_i - G_{i+1})\right)\right] \tag{3.22}$$

where G_i is the energy $G^{n,l}$ according to Eq. 3.19 for the current protonation state n and conformation l of system i. The parallel tempering procedure yields for each parallel copy a canonical ensemble at the corresponding temperature. Although the simulation of several ensembles is more costly, the tempering moves decrease the correlation within each ensemble and hence decrease the statistical error. Parallel tempering can also be used to improve the MC sampling of peptide conformations as described in chapter 2 (Hansmann, 1997).

In our MC simulations for the complete set of ensembles for all five myoglobin structures, we applied parallel tempering at the temperatures 300 K, 400 K, 533 K, 711 K and 948 K. For the evaluation of our results, we considered only the simulation data at 300 K. We added one tempering move

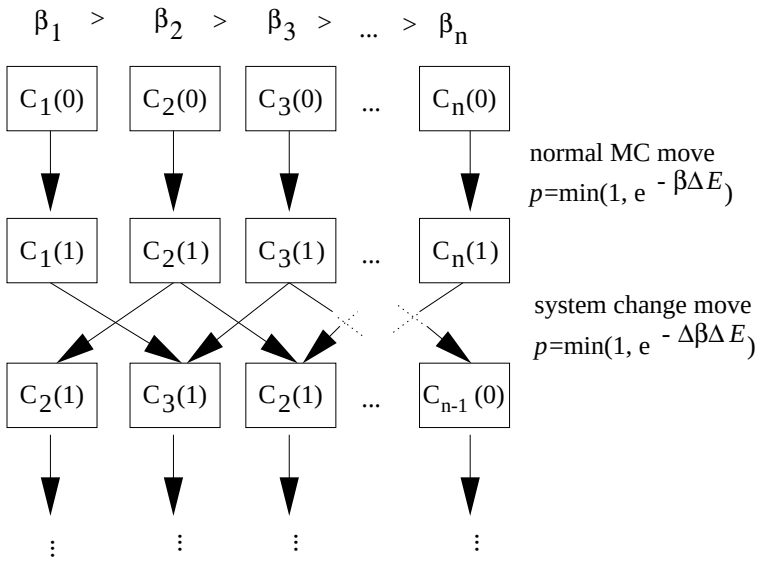

Figure 3.11: Scheme of an MC simulation with parallel tempering.

and ten conformational moves per MC scan of conventional titration moves. For each sampling, we performed 2,000 full scans and 100,000 reduced scans, leading to a statistical error (at 300 K) of less than 0.02 for the protonation probability of single groups, of less than 0.1 protons for the total protonation of myoglobin, and of less than 0.02 for the occupancy of individual conformations.

3.3.2.5 Conformational reference energy

For the MC sampling of the conformational ensemble, reasonable values for ΔG^l_{conf} are required. These values can in principle be obtained from a molecular dynamics force field like CHARMM (Rabenstein *et al.*, 1998a; Ullmann & Knapp, 1999), as this was done in section 3.2. However, it is unlikely that this method will give reasonable results in the case of the different MbCO structures. These structures are derived from crystallographic data and therefore inevitably involve small uncertainties in the atomic coordinates. Small structural changes within these uncertainties can change the energy value obtained from a force field dramatically. One could try to solve this problem by adjusting the structures according to the force field used, *e. g.* with an energy minimization. It is, however, questionable, in which way this should exactly be done without introducing an uncontrolled bias of the results. Therefore, we decided to use another method, where a modification of the given x-ray structures was not necessary.

First, we determined the ΔG^l_{conf} values only within the two alternative conformations in the x-ray structure from pH 4 (4a and 4b) and in the x-ray structure from pH 5 (5a and 5b), *i. e.* we simulated two-member ensembles consisting of 4a and 4b or of 5a and 5b. The occupancy of the two conformations was determined by the crystallographers to be 0.78 for 4a, 0.22 for 4b, 0.76 for 5a and 0.24 for 5b. Our aim was to find ΔG^l_{conf} values that reproduce these occupancies, denoted as α^l_{target}, in the multi-conformational MC sampling. We achieved this by an iterative method. We did first MC simulations (one for 4a/4b, one for 5a/5b) where the initial value of ΔG^l_{conf} was set to zero. The pH-value for these simulations were the same as those for the preparation of the x-ray structures, *i. e.* pH 4 for 4a/4b, pH 5 for 5a/5b. From the calculated occupancies α^l_{calc} of the conformations, a

correction energy ΔG^l_{corr} was derived by Eq. 3.23, which was added to ΔG^l_{conf}.

$$\Delta G^l_{corr} = RT \ln \frac{\alpha^l_{calc}}{\alpha^l_{target}} \tag{3.23}$$

If our initial MC sampling were not afflicted with a statistical error, the corrected values for ΔG^l_{conf} would be those we were looking for. However, there is a statistical error of α^l_{calc}, and the resulting error of ΔG^l_{corr} is especially large if α^l_{calc} is near to zero or unity. So we iteratively repeated the MC simulations with the corrected ΔG^l_{conf} values to get new values for ΔG^l_{corr}. We did this until the root mean square deviation (rmsd) of the calculated occupancies α^l_{calc} compared to the target occupancies α^l_{target} was smaller than 0.01, which was fulfilled after one to three iterations, depending on the calculation. For convenience, we shifted the ΔG^l_{conf} values additively after each iteration so that the shifted values for 4a and 5a were always zero. As shifted ΔG^l_{conf} values for the other conformations, we obtained 6.78 kJ/mol for 4b and -0.11 kJ/mol for 5b.

In the next step, we determined ΔG^l_{conf} values for the sampling of all conformations together. Again we applied an iterative method as before. The problem is, that values for the target occupancies are not directly available from experiment. Therefore, we assumed, that, averaged over the pH range from 3 to 7, all three groups of structures, 4a/4b, 5a/5b, and 6, are representing equally well the complete ensemble of the infinite number of possible myoglobin conformations. Hence, their occupancy integrated over this pH range should be equal (1/3). With this assumption, we could apply the iterative method as before with only a few modifications: The occupancy of a conformation α^l_{calc} is now calculated by integrating the calculated occupancy at a certain pH α^l_{pH} over the pH range from 3 to 7:

$$\alpha^l_{calc} = \int_{\mathrm{pH3}}^{\mathrm{pH7}} \alpha^l_{\mathrm{pH}} d\mathrm{pH} \tag{3.24}$$

For this calculation, the occupancies of 4a and 4b (or 5a and 5b, respectively) were always added together. Their relative ΔG^l_{conf} values were fixed to the values given above. The initial guess for the ΔG^l_{conf} values was -100 kJ/mol for 4a and -5 kJ/mol for 5a. The value for structure 6 was fixed to be zero. The resulting ΔG^l_{conf} values were -98.29 kJ/mol for 4a, -91.51 kJ/mol for 4b, -2.05 kJ/mol for 5a, -2.16 kJ/mol for 5b, and 0.00 kJ/mol for 6.

3.3.3 Results and Discussion

3.3.3.1 Population of the conformers

The calculated population probability of the conformers 4a, 4b, 5a, 5b, and 6 is plotted over the pH range from 3 to 7 in Fig. 3.12. Indeed, conformer 6 has its maximum population at the highest pH value and conformers 4a and 4b are most populated at the lowest pH value. Conformers 5a and 5b show a maximum of their population probability at intermediate pH values. For 5b, this maximum is located as expected at about pH 5, whereas for 5a, it is shifted to a higher pH of about 6. This difference is remarkable since the two conformers differ only at the residues Lys-79, Gly-80, and His-81 and the root mean square deviation (rmsd) is low (see Table 3.12). However, the shapes of the population curves of the corresponding conformer pair 4a and 4b differ less. Also the differences between 4a/4b and the other conformers is not surprising since there is a larger rmsd of about 1.1 Å and the extreme displacement of the His-64 sidechain. The conformational differences between 5a/5b and 6 are less pronounced, but nevertheless the shapes of their population curves are quite different.

In summary, we conclude that our method was able to calculate population probabilities of the MbCO conformers that are qualitatively correct and consistent with the experimental conditions of

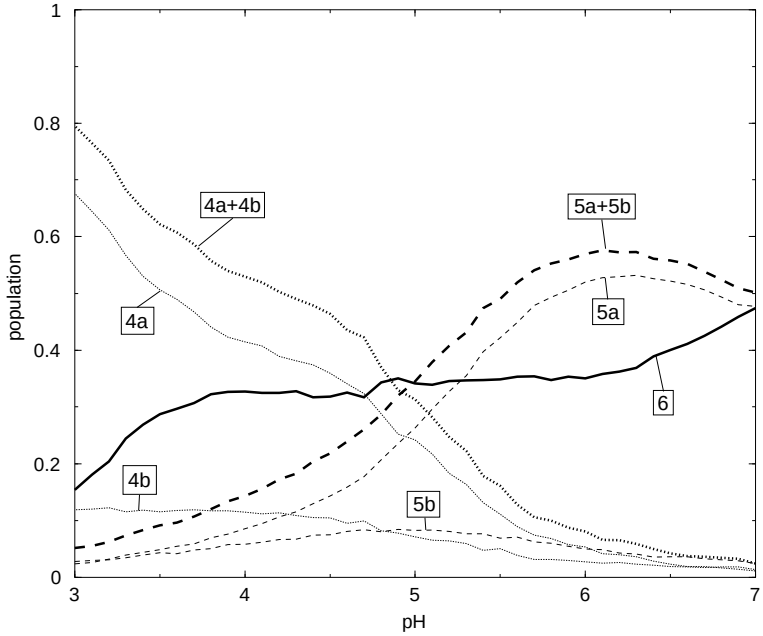

Figure 3.12: Calculated population probabilities of the different conformers in the pH range from 3 to 7.

Table 3.12: Root mean square deviations (rmsd) in Å for the five x-ray structures of MbCO considered in this work. Each two compared structures were aligned using the algorithm of Kabsch (1976).

	4a	4b	5a	5b	6
4a	0.00	0.20	1.09	1.07	1.07
4b	0.20	0.00	1.09	1.08	1.06
5a	1.09	1.09	0.00	0.16	0.63
5b	1.07	1.08	0.16	0.00	0.65
6	1.07	1.06	0.63	0.65	0.00

the x-ray structure determination. These population probabilities are sensitive to even small conformational changes.

3.3.3.2 Titration behavior of individual sites

Depending on the titratable site, the titration curves are more or less similar for the different conformations. For some sites, however, there are extreme differences. This is the case for His-64, which features the swing out of the CO binding pocket at low pH values. Fig. 3.13 shows the protonation

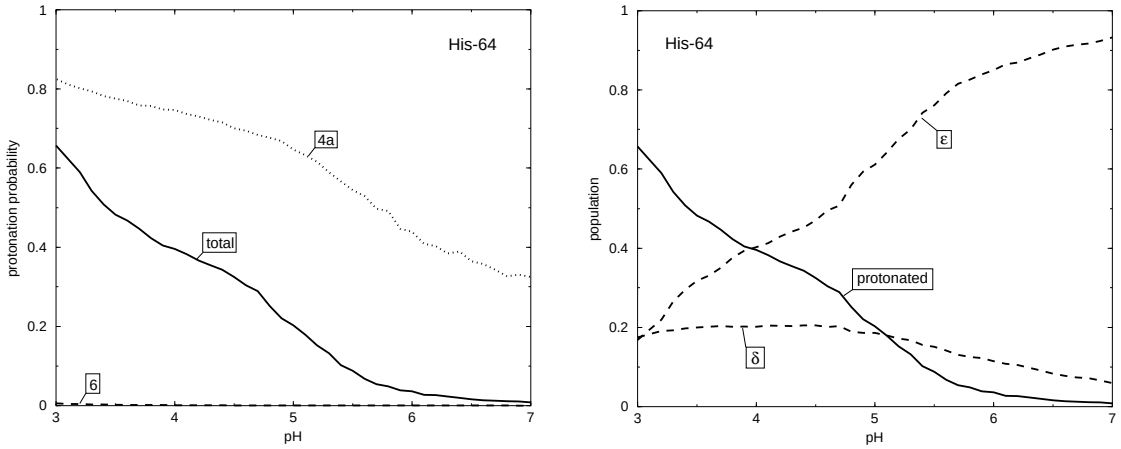

Figure 3.13: *Left panel:* Protonation probability of His-64 for the conformers 4a and 6, and for all conformers together (*total*). The protonation probabilities for the other conformers are not shown since they are very similar to 4a (4b) or 6 (5a and 5b). *Right panel:* Population probability of the tautomers of His-64, considering all conformers together.

probability of His-64 for different conformers. For the conformers 5a, 5b, and 6, His-64 is nearly unprotonated at all pH values. For the conformers 4a and 4b, where His-64 has swung out of the CO binding pocket, it is partially protonated, up to 80 % at low pH-values, but even at high pH-values nearly 50 %. If all conformers are considered together, the protonation of His-64 is closely correlated to the population probability of conformers 4a and 4b (Fig. 3.12) and thus with the rotation of His-64. This is in agreement with experimental findings (Yang & Phillips Jr., 1996). The δ-proton of the protonated His-64 in the 4a/4b-conformation is in hydrogen bond distance (1.8 Å) to the backbone oxygen of Asp-60. The distance of the δ-proton to the carboxy group of Asp-60, which is according to our results negatively charged at all pH values, is 3.7 Å. The hydrogen bond and the electrostatic attraction between the positively charged His-64 and the negatively charged Asp-60 may be responsible for pulling the protonated His-64 out of the binding pocket. In the conformers 5a, 5b, and 6, His-64 is not involved in any strong hydrogen bond with the protein moiety or the heme. (However, hydrogen bonding to water molecules in cavities of the protein is still possible. In the x-ray structure, water molecule 35 (structure 6) or water molecule 36 (structure 5a/b) is in hydrogen bond distance (3.1 Å or 2.7 Å, respectively) to N_δ of His-64.) In our calculations, we also determined the population probabilities for the two tautomers of histidine. Our result for His-64 is shown in Fig. 3.13. The unprotonated His-64 prefers the ε-tautomer, which is also reflected in Fig. 3.10 on page 67.

The titratable residues Lys-79 and His-81 are directly involved in the conformational difference between 5a and 5b, or 4a and 4b, respectively. Their titration behavior may be a key to understand the different shapes of the 5a and 5b population curves in Fig 3.12. Lys-79 is completely protonated for all considered pH-values and conformers. The titration behavior of His-81 is shown in Fig. 3.14. Although the titration curves for the conformers 4a and 4b are similar, the curves for 5a and 5b are much more different: The 5b curve resembles more the curves for 4a and 4b, whereas the 5a curve is

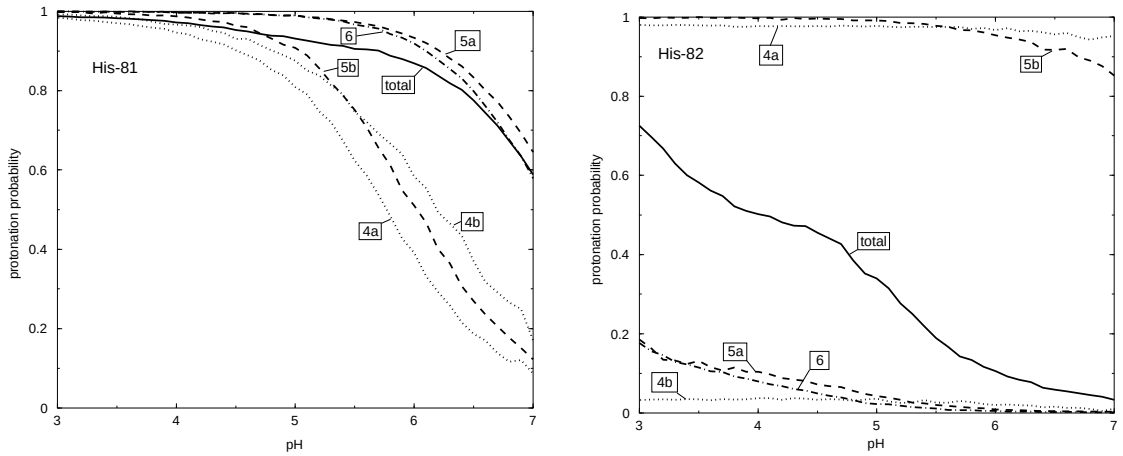

Figure 3.14: Protonation probability of His-81 (left) and His-82 (right) for the different conformers and all conformers together (*total*).

similar to the curve for conformer 6. There are extreme differences between the a and b conformations in both cases (4a/4b and 5a/5b) for the neighboring residue His-82 (Fig. 3.14). The titration curve of 4a is similar to that of 5b, and the titration curve of 4b is similar to that of 5a. So the curves are swapped between the more populated a conformations and the less populated b conformations.

3.3.3.3 The strongly coupled pair His-24/His-119

As discussed by Bashford *et al.* (1993), the ε nitrogen atoms of His-24 and His-119 are in hydrogen-bond distance and the two residues constitute a strongly coupled pair of titratable groups. During titration, they effectively share their ε-proton. Protonation of both residues at the same time practicallz does not occur. In the unprotonated state, His-24 adopts nearly completely the δ tautomeric form. The ε-tautomer of His-24 is nearly unpopulated. If and only if His-24 is protonated, His-119 adopts the δ tautomeric form. So only three states are practically occurring: pδ, δp, δε (Fig. 3.15). A "p" means protonated, "δ" represents the δ-tautomer, and "ε" the ε-tautomer. The first letter denotes the protonation state of His-24, the second that of His-119. The states pδ and δp are equivalent, if the ε-proton is considered as shared. This behavior is illustrated in Fig. 3.16.

3.3.3.4 Comparison of calculated pK_a values with experimental values and other theoretical studies

There are experimentally determined pK_a values for most of the histidines and tyrosines in MbCO. The values for Tyr-103 and Tyr-151 were determined by Wilbur and Allerhand (1976) to be 10.3 and 10.5, respectively. These values are out of the pH range we considered here (pH 3–7). According to our calculations, both tyrosine residues are protonated over the whole considered pH range. This is in agreement with the experimental findings.

More interesting is the comparison of the histidine values. They are listed in Table 3.13. Our calculated values are compared to experimental values and calculated values from other models. In the null model, the pK_a values are simply set to the pK_a values of the model compounds in aqueous solution. Here, the δ oder ε tautomer is chosen according to experimental results. In the uniform-80 model (Sandberg & Edholm, 1999), an electrostatic calculation is done with the dielectric constant uniformly set to $\varepsilon = 80$ everywhere. SCPB denotes a single-conformer Poisson-Boltzmann calculation (Bashford *et al.*, 1993). DaPDS (Distance and Position Dependent Screening) is a new method to calculate protonations states in proteins (Sandberg & Edholm, 1999). It is based on empirical

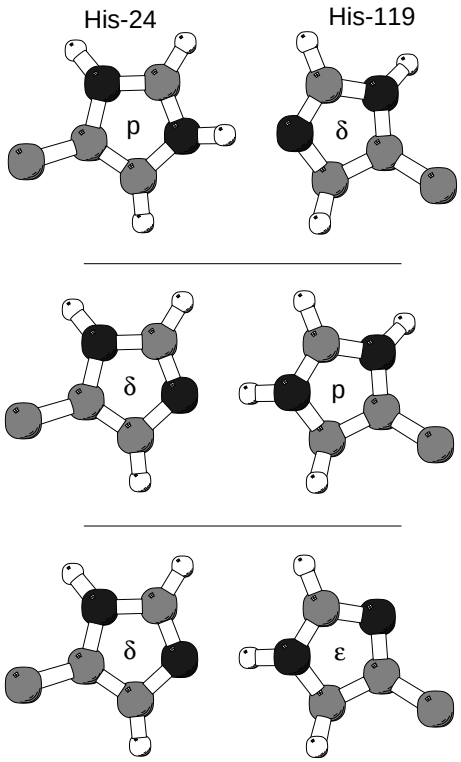

Figure 3.15: Structural representation of the of the strongly coupled pair His-24/His-119 with the three occurring protonation states pδ, δp, and δε explained in text.

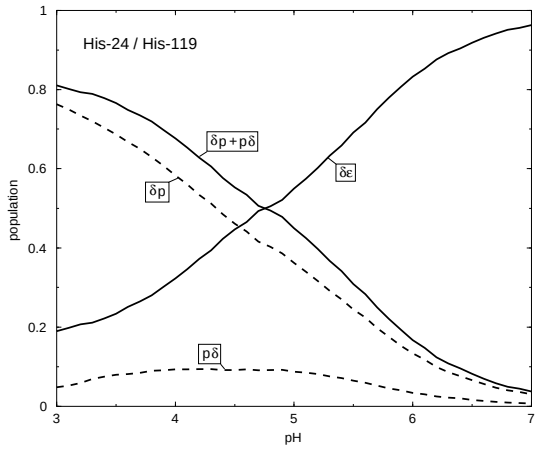

Figure 3.16: Population probabilities of the three possible states of the strongly coupled pair His-24/His-119 (see text). Since pδ and δp are considered to be equivalent, also their sum is shown.

Table 3.13: Experimental and calculated pK_a values of histidines in MbCO.

residue	experimental	calculated				
		null[1]	uniform 80[6]	SCPB[7]	DaPDS[8]	this work
His-12	6.3[3]	6.6	5.78	5.57	6.54	>7 (≈7.2[9])
His-24[2]	—	6.6	6.05	—	7.46	—
His-36	8.0[3]	7.0	6.89	6.24	7.27	>7
His-48	5.3[3]	6.6	6.16	4.79	6.74	5.09
His-64	<5[3] / 4.6[4]	6.6	5.63	-2.90	6.30	3.43
His-81	6.6[3]	7.0	6.81	6.87	7.21	>7 (≈7.1[9])
His-82	<5[3]	6.6	5.82	-2.29	6.60	4.04
His-97	5.6[3]	6.6	6.18	6.73	7.05	6.32
His-113	5.4[3]	6.6	4.96	4.26	6.08	4.36
His-116	6.5[3]	6.6	6.36	6.22	6.89	6.28
His-119[2]	6.1[3]	6.6	5.39	3.34	5.74	4.35
rmsd[5]	0.0	1.09	0.62	2.92	1.08	0.77

[1] unmodified pK_a values of model compound, δ or ε according to experimental results

[2] His-24 and His-119 are strongly coupled, see text

[3] Bashford *et al.* (1993)

[4] Fuchsman and Appleby (1979)

[5] compared to experimental values and including only residues printed in italics

[6] continuum electrostatics with $\varepsilon = 80$ everywhere (Sandberg & Edholm, 1999)

[7] Poisson-Boltzmann calculation similar to this work but with a single conformer (Bashford *et al.*, 1993)

[8] *Distance and Position Dependent Screening*, a simple electrostatic model (Sandberg & Edholm, 1999)

[9] extrapolated

screening functions (Warshel *et al.*, 1984) and is much simpler and thus faster than methods where the Poisson-Boltzmann equation must be solved. For each model, we calculated the rmsd compared to the experimental values. In the calculation of the rmsd, we included only histidine residues for which an experimental pK_a value in the range from 3 to 7 could be determined. In addition, we omitted the strongly coupled pair His-24 and His-119 due to their special titration behavior (s. a.), which does not allow to assign a well-defined pK_a value for each of these residues. That is also reflected in experimental findings (Bashford *et al.*, 1993). According to our results, His-12 and His-81 have pK_a values greater than 7, which is out of the range of our study. However, the point of half protonation is nearly reached at pH 7, so that we could extrapolate a pK_a value for these residues and include them in the rmsd calculation. The lowest rmsd value for the non-trivial models is reached with our method (Table 3.13). The low rmsd value of the uniform-80 model is not surprising since the experimental pK_a values are all not far from the model compound pK_a values and the uniform-80 model trivially provides pK_a values close to the model compound values. Especially interesting are the pK_a values for His-64, which performs the swing out of the binding pocket. The SCPB calculation (Bashford *et al.*, 1993), which used an x-ray structure prepared at intermediate pH (Kuriyan *et al.*, 1986), where His-64 is situated inside the CO binding pocket, shows a very low pK_a value as this is also implied by our calculation if only the conformers 6, 5a or 5b are considered (Fig. 3.13). If we consider the ensemble of all five conformers, the calculated pK_a value of His-64 is in reasonable agreement with the experimental result. The DaPDS calculation (Sandberg & Edholm, 1999) yields a high pK_a value for His-64 of 6.30 although it uses the same x-ray structure as the SCPB calculation, where His-64 is situated inside the CO binding pocket and should be mostly unprotonated. This constitutes an example where simple methods like the uniform-80 model or empirical models like DaPDS yield on the average results in reasonable agreement with experimental findings, but do not provide an understanding of the underlying molecular mechanism. The calculation of pK_a values by solving the PBE may sometimes run into difficulties and yield deviating results, but is capable to unveil what is going on in the more special situations, which may be crucial to understand protein function.

Bashford *et al.* (1993) reported a strong dependency of the Poisson-Boltzmann results on the used parameter set, *i. e.* atomic partial charges and atomic radii. They showed that choosing an appropriate parameter set can improve the reliability of the results significantly. The CHARMM22 parameter set, which was applied here, was not specifically designed for continuum electrostatics calculation, but rather for molecular dynamics at $\varepsilon = 1$ and with an explicit solvent (if any). So possibly our results could be improved even further, if the parameter set were tuned for continuum electrostatics calculations. However, our results presented here and also in another work (Vagedes *et al.*, 2000) suggests that the CHARMM22 parameter set is already quite well suited for continuum electrostatics calculations.

3.3.3.5 Implications for the assignment of taxonomic substates

Three taxonomic substates of MbCO can be distinguished by infrared spectroscopy: A_0, A_1, and A_3. A_0 is more populated at low pH, whereas A_1 and A_3 are present at higher pH (Johnson *et al.*, 1996). The A_0 substate is usually assigned to the protonated His-64 rotated out of the CO binding pocket (for further discussion see Johnson *et al.* (1996) and references cited therein). This assignment is also in agreement with our results. In general, A_1 is the dominant substate at pH 5.7 in solution (Johnson *et al.*, 1996). Ray *et al.* (1994) assigned A_1 to the ε-tautomer of His-64, and A_3 to the δ-tautomer. Jewsbury and Kitagawa (1994) criticized this assignment based on their MD simulations and suggested it the other way round, *i. e.* A_1 is the δ-tautomer and A_3 is the ε-tautomer. Our results, however, support the model of Ray *et al.* (1994) since the ε-tautomer is preferred at higher pH (Fig. 3.13 on page 74).